

TopoMortar: A dataset to evaluate image segmentation methods focused on topology accuracy

Juan Miguel Valverde^{1,2} Motoya Koga³ Nijihiko Otsuka³ Anders Bjorholm Dahl¹

¹Department of Applied Mathematics and Computer Science, Technical University of Denmark

²A.I. Virtanen Institute, University of Eastern Finland

³Department of Architecture Faculty of Engineering, Sojo University, Japan

Abstract

We present *TopoMortar*, a brick wall dataset that is the first dataset specifically designed to evaluate topology-focused image segmentation methods, such as topology loss functions. *TopoMortar* enables to investigate in two ways whether methods incorporate prior topological knowledge. First, by eliminating challenges seen in real-world data, such as small training set, noisy labels, and out-of-distribution test-set images, that, as we show, impact the effectiveness of topology loss functions. Second, by allowing to assess in the same dataset (*TopoMortar*) topology accuracy across dataset challenges, isolating dataset-related effects from the effect of incorporating prior topological knowledge. In these two experiments, it is deliberately difficult to improve topology accuracy without actually leveraging topology information, thus, permitting to attribute an improvement in topology accuracy to the incorporation of prior topological knowledge. To this end, *TopoMortar* includes three types of labels (accurate, pseudo-labels, noisy labels), two fixed training sets (large and small), and in-distribution and out-of-distribution test-set images. We compared eight loss functions on *TopoMortar*, and we found that *clDice* generally achieved the most topologically accurate segmentations, *Skeleton Recall* loss performed best particularly with noisy labels, and the relative advantageousness of the other loss functions depended on the experimental setting. Additionally, we show that simple methods, such as data augmentation and self-distillation, can elevate *Cross entropy Dice* loss to surpass most topology loss functions, and that those simple methods can enhance topology loss functions as well. *clDice* and *Skeleton Recall* loss, both skeletonization-based loss functions, were also the fastest to train, making this type of loss function a promising research direction. *TopoMortar* and our code can be found at <https://www.github.com/jmlipman/TopoMortar>.

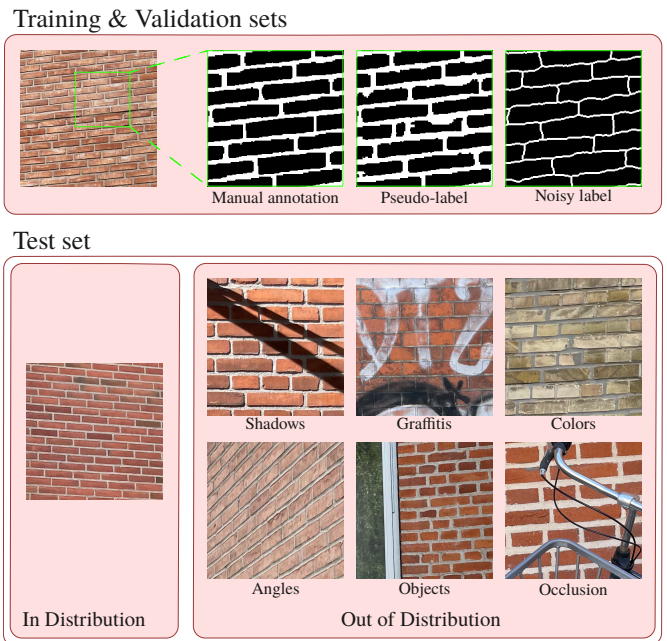


Figure 1. TopoMortar dataset.

1. Introduction

Deep learning has demonstrated extraordinary potential for image segmentation, yet even state-of-the-art models [27] cannot guarantee the connectivity of thin tubular structures, such as axons, vessels, and fibers. As a result, minor misclassifications can break the continuity of these structures, compromising their subsequent quantification. Topology loss functions (e.g., [20, 21, 45]) aim to address this issue by encouraging models to produce segmentations with the correct number of topological structures, such as connected components, holes, and hollows. However, their effectiveness is not completely well understood due to limitations in the datasets used to evaluate them.

Topology loss functions have been evaluated on datasets

with regions requiring precise connectivity, such as blood vessels. Datasets, in addition to their high-level segmentation task (*e.g.*, segmenting blood vessels on fundus retina images), present **challenges** that are rarely discussed or accounted for, such as class imbalance, small dataset size, noisy labels, pseudo-labels, and out-of-distribution (OOD) test-set images. The entanglement between dataset task and dataset challenges obscures when and where topology loss functions improve topology accuracy exclusively by means of incorporating prior topological knowledge. For instance, a method that addresses the same underlying challenge across different datasets (*e.g.*, Dice loss in class-imbalanced datasets) increases topology accuracy because it improves accuracy by tackling that particular challenge, however, it will not improve topology accuracy in similar datasets with other challenges. Thus, separating dataset task from dataset challenges to investigate methods’ **robustness** against such challenges allows to elucidate whether the methods have actually incorporated topological information [15].

Topology loss functions have not yet been evaluated on a dataset without challenges—likely, because such dataset does not exist. A challenge-free dataset would reduce the possibilities for methods to increase topology accuracy by exploiting dataset particularities or by indirectly tackling dataset challenges. Therefore, in such challenge-free dataset, an increase in topology accuracy can be attributed to the successful incorporation of prior topological knowledge. At the same time, it is unknown whether other simple, resource-friendly, well-established methods addressing dataset challenges can be more effective than topology loss functions, and whether topology loss functions can be further improved with such methods.

We present TopoMortar (Fig. 1), the first dataset specifically acquired for evaluating topology-focused image segmentation methods, such as topology loss functions. TopoMortar includes three types of labels (accurate, pseudo-labels, noisy labels), in-distribution (ID) and out-of-distribution (OOD) test-set images grouped into six categories, and two fixed training sets, allowing for experiments to investigate whether methods incorporate prior topological knowledge. In this work, we show that dataset challenges in previous datasets (small training set, noisy labels, pseudo-labels) affect differently the performance of topology loss functions. We also compared eight loss functions on TopoMortar, with and without those dataset challenges, and we found that cIDice was the only loss that consistently achieved the most topologically accurate segmentations, and that Skeleton Recall loss performed best with noisy labels. Our main contributions are:

- We release the first dataset to investigate whether methods incorporate prior topological knowledge by assessing model robustness against various real-world dataset challenges (small training set, noisy, pseudo-labels and OOD

images) and by reducing confounding factors (*i.e.* dataset particularities, such as those dataset challenges) that may also explain the increase in topology accuracy.

- We compare extensively, including statistical significance tests, one of the most popular objective function for image segmentation—Cross entropy Dice loss—with six topology and one non-topology loss functions.
- We show on TopoMortar that cIDice was the only evaluated topology loss function that improved topology accuracy across the majority of the experiments, indicating that it incorporates prior topological knowledge.
- We demonstrate that data augmentation and self-distillation can increase topology accuracy even when optimizing topology loss functions.
- We identify a type of topology loss function that is promising in terms of topology accuracy and computational demands: Skeletonization-based loss functions.

2. Related work

Topology loss functions have been evaluated on many different image segmentation datasets where the topology accuracy has been considered essential. The most used datasets across 28 related studies [2, 8, 10, 11, 16–18, 20–23, 26, 28–30, 36–38, 41, 43–46, 48, 50, 51, 53, 54] were DRIVE, Massachusetts Roads, and CREMI.

DRIVE [47] is a dataset of fundus retina images for blood vessel segmentation that has 20 training and 20 test images. The Massachusetts Roads dataset [35] consists of 1171 aerial images for road segmentation split into 1108, 14, and 49 training, validation, and test set images. CREMI dataset¹ is comprised by three 3D electron-microscopy images of the brain tissue of adult *Drosophila melanogaster*. Other datasets used to evaluate loss functions are CrackTree [56] (photographs of concrete cracks); ISBI12 [4] and ISBI13 [3] (electron-microscopy images of neurons); RoadTracer [5] and DeepGlobe [12] (aerial images of roads); and ACDC [7] and left ventricle UK biobank [40] (cardiac magnetic resonance images).

These datasets exhibit different challenges, making it difficult to conclude whether an increase in topology accuracy is due to the suitability to a particular task, due to the tackling of those dataset challenges, or due to the incorporation of prior topological information. The DRIVE dataset is extremely *small*; around one third of the training set images of the Massachusetts Roads dataset are *corrupted* (see Appendix A); The CREMI dataset only provides the instance segmentation of the neurons, thus, each study had to derive its own neuron borders *pseudo-labels*—a process that has not been documented and has been likely carried out differently (see Appendix B); CrackTree’s labels are one-pixel width lines (*i.e.*, *noisy labels*, see Ap-

¹<https://cremi.org>

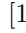

pendix C). On DRIVE—the most used dataset—previous studies have conducted 5-fold cross validation on the 20 training set images [26], 3-fold cross validation on 30 images [45], 3-fold cross-validation on the 20 training set images [21, 22], applied a 16-4-20 training, validation, and test set split [2, 17, 44], a 16-4 train-test split [30], or an unspecified split on the 20 training set images [20, 41]. This inconsistency is likely due to a combination of factors, including its small size, the lack of a fixed train-validation split, and the unavailability of the test-set labels. More details on the datasets and experimental discrepancies across studies can be found in Appendix D.

3. TopoMortar

Our dataset, TopoMortar is a brick wall dataset consisting of 420 RGB images of 512×512 pixels for the task of mortar segmentation. We have chosen brick walls with mortar because of the well-defined topological properties of the bricks and mortar. The mortar allows variation in the labels, and the brick walls are well suited for testing specific shifts in domain such as occluding objects, color change, etc. TopoMortar is split into a 50-20-350 train-validation-test set, with a second 10-image training set derived from the main 50-image training set. This split was chosen because TopoMortar includes seven groups of 50 images in the test set. TopoMortar contains manual annotations of the mortar for all images, and, for the training and validation sets, it also includes pseudo-labels and noisy labels (see Fig. 1 (top)). The training and validation sets contain images that align with the general concept of a red brick wall, *i.e.*, reddish bricks with mortar horizontally and vertically oriented and without any shadows or objects. The test set images are divided into seven groups: *in-distribution* brick walls that are similar to the training and validation sets; brick walls with *shadows* and *graffitis*; brick walls with bricks of different *colors*; brick walls images non-horizontally aligned taken from a different *angle*; and brick walls with *objects* in/next to them and objects *occluding* the walls. Figure 1 (bottom) shows an example of each category.

Data acquisition, processing, and split We took 195 photographs of brick walls and we manually cropped them into 823 512×512 non-overlapping patches that were, subsequently, divided into the seven categories described above. We then generated the training, validation, and test sets automatically, maximizing the diversity within each group (more details in Appendix E).

Labels We obtained the *pseudo-labels* for the in-distribution (ID) images by fitting the images into a Gaussian Mixture model of two components (mortar and brick). Since the mortar and bricks are grayish and reddish in the

majority of the images, we initialized the model with means $\mu_{mortar} = [119, 118, 123]$ , $\mu_{brick} = [107, 70, 71]$ . We then removed the connected components smaller than 300 pixels, and applied binary dilation followed by binary erosion. The manual annotations (*accurate* labels) for the ID images were obtained by carefully refining the pseudo-labels manually. For the out-of-distribution (OOD) images, a few models trained on TopoMortar’s training set were ensembled and the predictions were manually corrected. The manual annotation process took approximately 210 hours. Finally, we generated the *noisy labels* by skeletonizing the manual annotations and applying random elastic deformations and binary dilation, imitating rapid manual annotations with small human errors (see Figure 1).

Suitability for assessing topology accuracy TopoMortar allows to investigate in two ways whether methods incorporate prior topological knowledge: 1) by eliminating dataset challenges (*i.e.* confounding factors), and 2) by permitting to assess, on the same dataset, model robustness against various dataset challenges.

TopoMortar’s task is relatively simple (*i.e.*, mortar segmentation in red brick walls) which, in contrast to existing datasets that are more complex, an improvement in topology accuracy is less likely to be due to a more suitable choice of neural network, optimizer, training time, etc. TopoMortar also permits to eliminate typical challenges in real-world data (scarce training data, inaccurate labels, and OOD test-set images) by employing its large training set, accurate labels, and by measuring topology accuracy on the ID test set, thus, reducing confounding factors that could also explain an increase in topology accuracy. In such scenario without dataset challenges, a method has limited ability to exploit specific dataset characteristics to increase accuracy and, therefore, topology accuracy. In consequence, an improvement in topology accuracy can be attributed to the effective use of topological information.

TopoMortar can be configured to have the following dataset challenges: scarce training data, pseudo-labels, noisy labels, and OOD test-set images. By utilizing the same training set images (thus, fixing the dataset-related effects), an increase in topology accuracy across all challenges indicates the use of topology information. Since TopoMortar’s test set labels were manually refined, TopoMortar allows to measure topology accuracy more reliably than datasets with noisy/pseudo-labels that are in both the training and test set. TopoMortar’s OOD test set was deliberately designed to be difficult given the training set images, as it includes unseen scenarios with local and global differences in the intensity values (shadows, graffitis, colors), different brick orientations (angles), and the appearance of objects within, near, and occluding the brick walls (objects, occlusion). The *occlusion* category allows to assess whether

Loss	GPU (GiB)	Time (h.)
CEDice	5.6	2.3
RWLoss	5.6	14.5
TopoLoss	5.6	49.6
TOPO	5.9	28.8
clDice	16.2	3.1
Warping	5.6	152.1
SkelRecall	5.6	7.1
cbDice	7.8	58.3

Table 1. Computational requirements for training a nnUNet on TopoMortar for 12,000 iterations with a batch size of 10. Hardware: Intel Xeon Gold 6126, NVIDIA Tesla V100 (32GB).

the evaluated methods can connect structures that appear unconnected and, we know, are actually connected. This is particularly relevant for amodal segmentation, where the goal is to predict the complete structure even when parts are occluded or hidden. Thus, this category helps to elucidate whether the model has gained information about the true topology of the structures, which is essential for segmenting, , *e.g.*, roads in aerial images occluded by trees, myelin in electron-microscopy images with debris, and structures in medical images with limited resolution (see Appendix F).

TopoMortar is built to address previous dataset limitations and to avoid discrepancies in the experimental settings of future studies. To this end, TopoMortar includes 1) a fixed training-validation-test set, 2) two fixed training sets, 3) accurate, noisy, and pseudo-labels for the training and validation sets, 4) the manual annotations of all the images, and 5) several OOD test set images (85% of the test set) divided into six groups portraying different challenges. Additionally, the comparatively small size of TopoMortar’s images (512×512 pixels) lessens GPU memory requirements, thereby offering ample capacity for methods with high memory demands. TopoMortar is larger than most datasets used in previous related studies (Appendix D). As our experiments demonstrate, its large training set consisting of 50 images suffices to achieve significantly higher topology accuracy than the small training set, allowing to study whether topology losses advantageousness decreases when increasing the training set size. Moreover, unlike in most datasets that focus on either 0-dimensional topological structures (connected components) or 1-dimensional topological structures (holes), in TopoMortar both topological structures are relevant, as they correspond to the mortar and bricks, respectively.

4. Experiments

We conducted four sets of experiments. First, we investigated the impact of dataset challenges and limitations on the effectiveness of topology loss functions in datasets used by previous work. Second, we compared topology loss functions on TopoMortar in a setup without dataset chal-

lenges. Third, we compared topology loss functions across different dataset challenges. Fourth, we studied the extent to which two simple non-topology-focused methods for tackling dataset challenges (data augmentation and self-distillation) can improve topology accuracy.

Loss functions We compared eight loss functions, including six topology loss functions, with different characteristics. *Non-topology loss functions*: The combination of Cross entropy and Dice loss (CEDice), which are the most utilized loss functions in image segmentation; RegionWise loss [49], that is based on distances to the structures’ borders and has been shown to improve topology accuracy [31]. *Persistence-homology-based loss functions*: TopoLoss [21], that finds via persistence homology [14] the pixels that lead to topological errors. *Distance-maps-based topology loss functions*: TOPO [37] and Warping loss [22], that employ distance maps to identify the critical areas that change the topology of the segmentations. *Skeletonization-based loss functions*: clDice [45], Skeleton Recall [26], and cbDice [44], that focus on the accuracy of the segmentations’ skeletons.

Optimization All our experiments were run with 10 different random seeds, providing us with sufficient measurements to evaluate the significance of performance differences. For this, we computed paired permutation tests with 10,000 random iterations. We optimized nnUNet [24] for 12,000 steps with stochastic gradient descent, with a starting learning rate of 0.01, nesterov momentum of 0.99, and polynomial learning rate decay. We applied several data augmentation transformations, including random rotations, scaling, and Gaussian noise. All details about the optimization can be found in Appendix G. We implemented our experiments in MONAI [9] and PyTorch [39], and we ran our experiments in two clusters with several Tesla A100, V100, A10, and A40, ranging from 16 to 40 GB of GPU memory.

Metrics We computed the Betti errors, defined as the differences in Betti numbers between the ground truth and the segmentation. The Betti 0 error (β_0) refers to the difference in the number of connected components, while the Betti 1 error (β_1) refers to the difference in the number of holes (in most cases corresponding to the bricks in TopoMortar). Additionally, we calculated the Dice coefficient [13] and Hausdorff distance (95th percentile) [42] which are standard metrics in image segmentation that measure the overlap between the ground truth and the segmentation, and the distance to the farthest misclassification, respectively.

4.1. Challenges and limitations in previous datasets

We investigated the challenges and limitations in the datasets previously used to evaluate topology loss functions.

		Betti error		Dice	
		D.A.	No D.A.	D.A.	No D.A.
CREMI	CEDice	2371 ± 1046	1356 ± 1126	0.81 ± 0.0	0.75 ± 0.0
	RWLoss	3008 ± 1008	1039 ± 1145	0.79 ± 0.01	0.77 ± 0.0
	TopoLoss	1898 ± 1090	3393 ± 1206	0.81 ± 0.0	0.75 ± 0.0
	TOPO	16140 ± 30223	20327 ± 1687	0.63 ± 0.22	0.78 ± 0.0
	clDice	2904 ± 635	6421 ± 1253	0.77 ± 0.0	0.76 ± 0.0
	Warping	3795 ± 998	1270 ± 620	0.8 ± 0.0	0.76 ± 0.0
	SkelRecall	2519 ± 1323	2003 ± 1198	0.75 ± 0.01	0.75 ± 0.0
	cbDice	3407 ± 951	2934 ± 1460	0.81 ± 0.0	0.76 ± 0.0
			DRIVE	FIVES	DRIVE
Supervised	CEDice	172.42 ± 15.7	43.79 ± 6.74	0.72 ± 0.0	0.89 ± 0.0
	RWLoss	159.38 ± 15.4	163.9 ± 17.78	0.74 ± 0.0	0.76 ± 0.01
	TopoLoss	67.54 ± 8.1	42.51 ± 7.15	0.73 ± 0.0	0.86 ± 0.0
	TOPO	221.6 ± 37.08	76.83 ± 16.51	0.72 ± 0.01	0.81 ± 0.01
	clDice	61.04 ± 8.89	16.99 ± 3.97	0.73 ± 0.0	0.86 ± 0.0
	Warping	115.62 ± 11.38	53.41 ± 7.11	0.73 ± 0.0	0.88 ± 0.0
	SkelRecall	128.86 ± 15.28	37.75 ± 6.98	0.72 ± 0.0	0.83 ± 0.01
	cbDice	116.32 ± 12.02	55.69 ± 7.77	0.73 ± 0.0	0.87 ± 0.0
			Supervised	Adele	Supervised
CrackTree	CEDice	84.3 ± 9.66	51.97 ± 7.56	0.78 ± 0.01	0.75 ± 0.01
	RWLoss	-	-	-	-
	TopoLoss	145.82 ± 18.18	134.87 ± 19.59	0.52 ± 0.02	0.47 ± 0.02
	TOPO	-	-	-	-
	clDice	22.13 ± 28.54	18.03 ± 37.17	0.54 ± 0.12	0.34 ± 0.08
	Warping	94.85 ± 10.71	46.37 ± 7.35	0.77 ± 0.01	0.73 ± 0.01
	SkelRecall	14.03 ± 8.82	24.62 ± 8.31	0.32 ± 0.01	0.3 ± 0.01
	cbDice	84.64 ± 8.33	66.49 ± 9.3	0.76 ± 0.01	0.69 ± 0.01

Table 2. Mean and std. of Betti errors in previous datasets. Top: β_1 error on CREMI dataset, with vs. without data augmentation. Center: β_0 error in standard supervised training, DRIVE vs. FIVES datasets. Bottom: β_0 error on CrackTree dataset, standard supervised learning vs. Adele. **Bold:** Betti errors are lower and significantly different than CEDice loss.

Such challenges and limitations were: CREMI’s unsuitability to estimate reliable β_1 errors and lack of true labels, DRIVE’s small dataset size, and CrackTree’s noisy labels.

CREMI is unsuitable for quantifying β_1 errors

CREMI is an electron-microscopy dataset comprised of three 3D images whose labels were automatically generated from the border of the instance segmentation of the axons. We divided this dataset into one image for training, one for validation, and one for testing, and we compare all loss functions, with and without data augmentation.

The only loss functions that achieved smaller and significantly different β_1 errors than CEDice were TopoLoss and RWLoss (see Table 2, “CREMI”). However, since CREMI’s pseudo-labels had many holes and the Betti errors only focus on their number, automatic segmentations with numerous holes, including incorrect ones, will show lower β_1 errors. In consequence, a decrease in the β_1 error does not guarantee higher topology accuracy; instead, it might indicate that the segmentation had more incorrect holes (see Appendix H). Data augmentation, which is heavily under-reported in the literature (Appendix D), was crucial to improve accuracy. Furthermore, we could make any loss function appear as the best by carefully selecting a random seed (Appendix I).

DRIVE’s small dataset Blood vessel segmentation in fundus retina images is an important task that can benefit from topology-focused image segmentation methods. However, the DRIVE dataset [47]—the most popular dataset among topology loss function studies—introduces an extra challenge due to its small size, making it unclear whether topology loss functions are beneficial on this particular task or on datasets of small size. To answer this question, we compared topology loss functions on DRIVE (13-2-5 train-validation-test split) alongside FIVES [25] (538-60-200 split), which is a similar but much larger dataset.

On the DRIVE dataset, six loss functions achieved smaller and significantly different β_0 errors than CEDice, whereas, on FIVES, only three of them achieved smaller and significantly different β_0 errors (Table 2, “Supervised”), demonstrating the impact of scarce data on topology accuracy. Loss functions generally performed better on the FIVES dataset, with CEDice gaining a nearly $\times 4$ improvement in the β_0 error—the largest. Additionally, while the Dice coefficients were similar across loss functions within the same dataset, the β_0 errors varied considerably. clDice achieved the most topologically accurate segmentations on both datasets, and the relative effectiveness of the other loss functions varied. For instance, Skeleton Recall was only the 5th most accurate loss on DRIVE, but the 2nd on FIVES.

CrackTree’s noisy labels

CrackTree [56], designed for the segmentation of concrete cracks, includes labels annotated with one-pixel width lines (see Appendix C). Thus, this dataset introduces the challenge of learning from imperfect labels. Here, we compared optimizing the topology loss functions via standard supervised learning, which is suboptimal for this type of labels, and via Adele [32], which is a method designed for training deep learning models with noisy labels. We divided CrackTree into a 147-17-42 train-validation-test split and we tackled class imbalance by multiplying the loss on each class by [0.2, 0.8].

All topology loss functions improved their topology accuracy when optimized via Adele (Table 2, “CrackTree”), except Skeleton Recall loss that even with standard supervised learning it achieved the lowest β_0 errors. RWLoss and TOPO led to empty masks. Since the test-set labels are also noisy, the Dice coefficients hardly reflected segmentation quality. For instance, clDice and Skeleton Recall, which achieved the lowest Dice coefficients, produced thick segmentations that corresponded better to the exact location of the concrete cracks than the ground truth (Appendix C). In general, Adele led all loss functions to produce thicker segmentations, decreasing their Dice coefficients.

4.2. Benchmark on TopoMortar without challenges

We evaluated topology loss functions on TopoMortar on a setup without dataset challenges, thus, **reducing the con-**

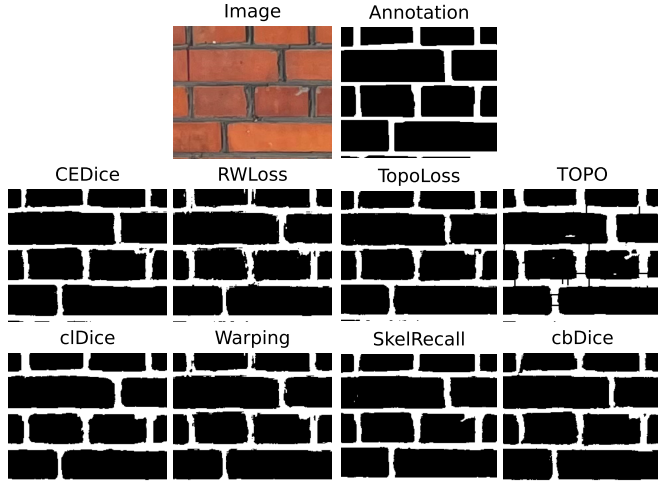


Figure 2. Segmentations on the in-distribution image where the β_1 error was, on average, the highest. Training setup: Typical supervised learning, full training set, accurate labels.

founding factors that could lead to an increase in topology accuracy without incorporating prior topological knowledge. To this end, we trained on TopoMortar’s *large* training set with *accurate* labels, and we separated the performance measurements in the test set between *ID* and *OOD*. In other words, in this experiment, we accounted for no dataset challenges, as prior topology loss function studies, but, differently from those studies, we ensured our dataset had no such challenges, which, as we showed, affect topology accuracy. On top of the Betti errors, Dice coefficient, and HD95, we also measured local topology accuracy by computing the Betti error in a 128×128 sliding window.

clDice and Skeleton Recall were the only loss functions that achieved Betti errors lower and significantly different than CEDice on both the ID and OOD test-set images (see Table 3). In the ID test set, CEDice, TopoLoss, and Skeleton Recall produced segmentations with the second lowest β_0 errors, which, between them, were not significantly different. In the OOD test set, TopoLoss and TOPO also achieved lower and significantly different β_0 errors than CEDice, while Warping did similarly on the β_1 error. TOPO’s low β_0 errors in the OOD dataset were due to over-segmentation, especially in the bricks with different colors (see Appendix J, “colors”). The Dice coefficients and HD95 were similar across loss functions and, although they did not reflect segmentation quality too accurately, they signaled whether a loss function did not produce satisfactory segmentations (see TOPO in Table 3 (ID test set and Dice, and OOD test set and HD95)). Since the local Betti errors were highly correlated to β_0 and β_1 errors (Pearson correlation > 0.98), we did not include them in the paper.

	Loss	β_0 error	β_1 error	Dice	HD95
ID test set	CEDice	3.31 \pm 2.62	2.13 \pm 1.02	0.91 \pm 0.00	1.87 \pm 0.03
	RWLoss	5.72 \pm 1.65	6.03 \pm 2.15	0.91 \pm 0.00	1.84 \pm 0.01
	TopoLoss	3.14 \pm 1.80	2.73 \pm 3.37	0.91 \pm 0.0	1.87 \pm 0.03
	TOPO	33.69 \pm 4.65	43.35 \pm 3.44	0.86 \pm 0.00	2.68 \pm 0.18
	clDice	1.17\pm0.54	1.41\pm0.59	0.91 \pm 0.00	1.83 \pm 0.01
	Warping	4.20 \pm 2.04	3.62 \pm 1.16	0.91 \pm 0.00	1.84 \pm 0.01
	SkelRecall	3.08 \pm 1.41	1.73\pm0.77	0.91 \pm 0.00	1.90 \pm 0.03
	cbDice	4.24 \pm 2.08	3.81 \pm 2.28	0.91 \pm 0.00	1.85 \pm 0.02
OOD test set	CEDice	197.25 \pm 24.21	87.81 \pm 21.32	0.65 \pm 0.01	37.65 \pm 1.20
	RWLoss	219.55 \pm 28.45	87.74 \pm 19.22	0.64 \pm 0.01	37.31 \pm 1.29
	TopoLoss	193.29\pm47.92	99.33 \pm 28.05	0.65 \pm 0.01	37.33 \pm 1.06
	TOPO	117.73\pm19.37	105.09 \pm 24.71	0.65 \pm 0.01	40.21 \pm 0.81
	clDice	81.33\pm13.16	51.64\pm7.34	0.66 \pm 0.01	36.90 \pm 1.29
	Warping	204.26 \pm 26.69	80.23\pm18.01	0.65 \pm 0.01	37.07 \pm 1.25
	SkelRecall	180.23\pm24.44	96.79 \pm 30.14	0.67 \pm 0.01	38.46 \pm 1.02
	cbDice	233.49 \pm 34.09	106.08 \pm 33.24	0.65 \pm 0.01	37.84 \pm 1.16

Table 3. Average performance (10 random seeds) on TopoMortar test set, separated into in-distribution (ID) and out-of-distribution (OOD) images. Training setup: Standard supervised learning, large training set, accurate labels. **Bold:** Betti errors are lower and significantly different than CEDice loss.

4.3. Robustness to scarce training data, low-quality labels, and OOD images

We investigated on TopoMortar whether and to what degree existing topology loss functions enhance model **robustness** against scarce training data, inaccurate labels, and OOD images. Studying model robustness by disentangling the different types of dataset challenges and other dataset-related factors allows to elucidate if topology loss functions incorporate prior topological knowledge, as incorporating prior knowledge, in theory, increases model robustness [15]. First, we compared topology loss functions in a scarce training data setup (as in DRIVE) by using TopoMortar’s *small* training set. Second, we compared them in a setup with labels generated semi- or fully automatically (as in CREMI) by using TopoMortar’s *pseudo-labels*. Third, we compared topology loss functions in a setup with inaccurate labels resulting from a quick approximated human annotation (as in CrackTree) by using TopoMortar’s *noisy labels*. Additionally, we separate the measurements distinguishing between ID and OOD test-set images. In all the experiments, we trained the models via standard supervised learning and, unless otherwise specified, we employed TopoMortar’s large training set and accurate labels.

The models’ performance decreased considerably after introducing the aforementioned dataset challenges, with an average Dice coefficient in the ID test set of 0.90, 0.86, and 0.68 in the scarce training data, pseudo-label, and noisy label setups, respectively (Appendix L). On both ID and OOD test sets, clDice achieved the lowest Betti errors when training on the small training set and when training on pseudo-labels, whereas Skeleton Recall loss was generally superior with noisy labels (Table 4). The second best topology

Test set →	β_0 error		β_1 error		
	ID	OOD	ID	OOD	
Small training set	CEDice	9.57 \pm 4.36	182.01 \pm 15.72	4.63 \pm 3.31	61.51 \pm 8.63
	RWLoss	12.35 \pm 7.17	201.0 \pm 16.71	6.42 \pm 2.80	56.53\pm11.51
	TopoLoss	8.72\pm2.95	152.05\pm13.56	4.81 \pm 5.06	58.13\pm8.89
	TOPO	59.6 \pm 20.01	312.12 \pm 34.32	43.29 \pm 3.53	109.61 \pm 30.14
	clDice	6.18\pm6.23	127.32\pm14.48	4.01\pm3.02	38.70\pm7.93
	Warping	11.37 \pm 6.51	190.2 \pm 19.76	4.53\pm2.84	43.59\pm11.63
	SkelRecall	9.89 \pm 3.43	160.08\pm11.97	5.18 \pm 3.93	69.23 \pm 10.37
	cbDice	9.60 \pm 4.70	156.88\pm15.33	4.92 \pm 2.92	54.75\pm8.33
	Pseudo-labels	CEDice	12.26 \pm 1.45	126.21 \pm 25.99	12.00 \pm 1.54
RWLoss		11.38\pm1.43	114.65\pm24.6	11.11\pm1.99	96.49 \pm 23.22
TopoLoss		10.43\pm1.11	117.98\pm15.44	10.13\pm1.36	110.32 \pm 32.74
TOPO		36.09 \pm 5.10	225.37 \pm 36.65	31.10 \pm 2.76	132.21 \pm 40.97
clDice		1.80\pm0.44	32.70\pm6.07	4.30\pm0.37	61.57\pm12.4
Warping		13.57 \pm 1.68	127.08 \pm 39.30	13.26 \pm 2.33	95.47 \pm 19.71
SkelRecall		10.40\pm1.63	113.63\pm25.35	10.43\pm1.66	85.75 \pm 20.50
cbDice		13.12 \pm 3.54	141.42 \pm 33.27	14.66 \pm 2.54	122.91 \pm 48.20
Noisy labels		CEDice	6.24 \pm 1.05	175.17 \pm 14.42	5.08\pm0.56
	RWLoss	17.90 \pm 3.73	427.46 \pm 25.66	11.93 \pm 0.96	17.87\pm3.08
	TopoLoss	7.19 \pm 2.46	205.05 \pm 11.75	6.62 \pm 0.43	14.84\pm1.26
	TOPO	24.14 \pm 9.42	157.22\pm32.35	10.93 \pm 4.75	140.45 \pm 21.72
	clDice	5.01\pm0.49	126.52\pm13.09	6.77 \pm 0.50	48.20 \pm 15.50
	Warping	8.48 \pm 1.70	285.20 \pm 19.06	9.49 \pm 0.62	18.01\pm1.75
	SkelRecall	3.79\pm1.57	113.33\pm13.53	1.49\pm0.38	44.60 \pm 7.85
	cbDice	10.50 \pm 1.43	275.69 \pm 14.26	9.74 \pm 0.63	27.50 \pm 6.60

Table 4. Average performance on TopoMortar test set. Top: training setup as in Table 3 but with the small training set. Center: Pseudo-labels. Bottom: Noisy labels. **Bold**: Significantly lower than CEDice. **Red**: Smallest average. **Blue**: Second smallest.

loss function depended on the experimental setup and the Betti error (Table 4, blue). In the OOD test set, according to the β_0 error, TopoLoss was the second best in the small training set setup, Skeleton Recall in the pseudo-labels, and clDice in the noisy-labels experiment. According to the β_1 error, Warping loss in the small training set, CEDice in the pseudo-labels, and RWLoss in the noisy-labels experiment.

4.4. Topology losses with data augmentation and self-distillation

We studied the impact on topology accuracy of two simple methods for tackling dataset challenges. First, we accounted for the presence of OOD images with a simple *data augmentation* method that increased the colors’ diversity in the images and that we applied with a probability of 50%. This data augmentation, that we refer to as *RandHue*, converted the images to the HSV color space; randomly chose the same hue for all pixels; randomly shifted the saturation and value; and converted the image back to RGB (see examples in Appendix M). Second, we accounted for labels being pseudo-labels and noisy labels by training with *self-distillation* [19]—a strategy known to be advantageous with those types of labels. We employed self-distillation due to its simplicity and because it incorporated no extra hyperparameters. To keep the total iterations to 12,000 as in all our experiments, we trained the models for 4,000 iterations,

Test set →	β_0 error		β_1 error		
	ID	OOD	ID	OOD	
D.A. (RandHue)	CEDice	1.90\pm2.88	69.73 \pm 14.88	1.99 \pm 4.98	53.32 \pm 11.63
	RWLoss	3.30 \pm 0.98	62.75\pm5.78	2.93 \pm 1.92	49.84\pm3.62
	TopoLoss	2.87 \pm 4.22	85.25 \pm 20.41	3.34 \pm 7.8	80.09 \pm 18.66
	TOPO	19.71 \pm 2.34	97.24 \pm 11.22	40.56 \pm 1.42	49.91\pm10.55
	clDice	0.56\pm0.22	16.54\pm3.06	0.95\pm0.13	15.12\pm2.56
	Warping	2.50 \pm 1.33	57.07\pm5.79	1.88 \pm 1.26	40.02\pm3.67
	SkelRecall	2.00 \pm 2.80	65.46 \pm 8.74	2.01 \pm 4.77	62.72 \pm 9.31
	cbDice	2.71 \pm 1.18	90.26 \pm 17.74	3.29 \pm 4.70	83.22 \pm 17.50
	Pseudo + Self. dist.	CEDice	3.76\pm0.38	68.35 \pm 14.25	3.99 \pm 0.50
RWLoss		4.43 \pm 0.35	72.95 \pm 13.09	4.27 \pm 0.51	43.88\pm8.64
TopoLoss		7.57 \pm 1.38	34.87\pm6.6	3.55\pm0.39	31.74\pm6.66
TOPO		64.52 \pm 9.87	131.26 \pm 19.15	73.08 \pm 6.52	57.51 \pm 41.14
clDice		2.13\pm0.37	32.55\pm2.35	2.69\pm0.34	55.92\pm10.31
Warping		4.58 \pm 0.48	66.29\pm5.58	4.82 \pm 0.46	42.68\pm7.42
SkelRecall		4.72 \pm 0.40	81.54 \pm 16.63	5.44 \pm 0.55	61.77 \pm 15.25
cbDice		4.50 \pm 0.57	78.42 \pm 14.11	4.79 \pm 0.48	61.37 \pm 19.26
Noisy + Self. dist.		CEDice	2.43 \pm 0.71	113.55 \pm 9.41	2.79 \pm 0.38
	RWLoss	13.48 \pm 1.95	288.58 \pm 22.51	16.62 \pm 1.52	17.93 \pm 0.75
	TopoLoss	5.57 \pm 1.72	112.54 \pm 10.74	8.28 \pm 1.32	15.73\pm0.72
	TOPO	67.23 \pm 45.70	118.35 \pm 35.49	9.25 \pm 6.28	81.03 \pm 26.45
	clDice	0.91\pm0.30	62.84\pm9.61	1.64\pm0.22	22.54 \pm 3.00
	Warping	2.75 \pm 0.33	153.22 \pm 10.62	4.00 \pm 0.40	16.17 \pm 1.79
	SkelRecall	1.43\pm0.50	62.77\pm8.54	0.97\pm0.13	36.82 \pm 7.71
	cbDice	4.74 \pm 1.00	163.05 \pm 12.79	6.25 \pm 1.18	23.56 \pm 27.87

Table 5. Average performance on TopoMortar test set. Top: training setup as in Table 3 but with data augmentation (*RandHue*). Center: Pseudo-labels and self-distillation. Bottom: Noisy labels and self-distillation. **Bold**: Significantly lower than CEDice. **Red**: Smallest average. **Blue**: Second smallest.

generated soft labels for the training set, trained on those labels for another 4,000 iterations, and repeated the process one more time.

The segmentations and, particularly, their topology accuracy were generally better than in the previous experiment where no dataset challenge was directly tackled. clDice also achieved the best segmentations in most cases, and Skeleton Recall also outperformed in the presence of noisy labels. As in the previous experiment, the second-best topology loss function depended on the specific experimental setup. Applying *RandHue* improved the Dice coefficients in the OOD images and decreased the Betti errors significantly in both the ID and OOD test set (Table 3 vs. Table 5 (top)). The decrease in the β_0 error occurred across all OOD groups, whereas the decrease in the β_1 error occurred only in “angles”, “colors”, and “shadows” (see Appendix N). When training on pseudo-labels and noisy labels, self-distillation improved the Dice coefficients and topology accuracy, especially in the OOD images and except on TOPO loss.

5. Discussion

We presented TopoMortar, a dataset specifically created to study the effectiveness of topology-focused image segmentation methods. We showed that existing datasets exhibit challenges that were not previously considered and that in-

fluence topology accuracy. We compared eight loss functions on TopoMortar on a setup without dataset challenges and then studied model robustness in the presence of those challenges. Finally, we investigated the extent to which simple data augmentation and self-distillation can increase topology accuracy.

We evaluated topology loss functions on different datasets, following the standard experimental approach. Additionally, we tackled the challenges of data scarcity and noisy labels in DRIVE and CrackTree datasets with a larger dataset and with a method to learn from noisy labels, respectively. Our experiments revealed two key points. First, no topology loss function was the best across all settings, which contrasts with topology loss function studies where the proposed loss function always outperforms the others. Second, by tackling dataset challenges, not only topology accuracy improves but also the relative advantageousness of the topology loss functions changes. Importantly, this experiment **does not reveal when and why** specific topology loss functions are advantageous, as comparing across datasets entangles dataset tasks and dataset challenges. For instance, cbDice and Warping loss achieved higher topology accuracy than CEDice in the DRIVE dataset while, on CrackTree, they did not surpass CEDice. This may indicate that cbDice and Warping loss lead to models robust against scarce training data but not against noisy labels; or that cbDice and Warping loss are particularly well suited for blood vessel segmentation; or both.

We evaluated the topology loss functions on TopoMortar **eliminating dataset challenges** by ensuring sufficient training data, training time, accurate labels, ID test-set images, strong data augmentation, and a state-of-the-art deep learning model. This scenario was either assumed or not discussed in previous works. Using TopoMortar, we reduced the dataset particularities that could have helped in increasing topology accuracy without incorporating topology information as, *e.g.*, Dice loss would do in class-imbalanced datasets. In this challenging setup, cIDice and Skeleton Recall achieved β_1 errors smaller and significantly different than CEDice, with cIDice also achieving smaller and significantly different β_0 errors, demonstrating the potential of skeletonization-based topology loss functions.

We investigated model **robustness** against dataset challenges after optimizing topology loss functions on TopoMortar. In contrast to experiments on other datasets, TopoMortar allows to fix dataset task (*i.e.*, segmenting mortar in red brick walls), permitting to study the effect of each dataset challenge, individually, on the potential advantageousness of topology losses. We observed 1) that cIDice was generally the best-performing loss, 2) that Skeleton Recall worked best specifically under the presence of noisy labels, and 3) that the performance of the other losses varied depending on the dataset challenge. These results, in

line with the other experiments, indicate that cIDice truly incorporates topology information to the models. The out-performance of Skeleton Recall over cIDice on noisy labels can be explained by its emphasis on the foreground region (true positives, false negatives), as, on the TopoMortar noisy labels, the foreground corresponds to a thicker and more accurate skeleton than what cIDice produces. Thus, it may be that with a different type of noisy labels [1] Skeleton Recall performs differently.

We also studied the impact of data augmentation and self-distillation on topology accuracy. These simple and well-established strategies improved the baseline CEDice when training on a large training set with accurate labels and when optimizing on noisy and pseudo-labels (Tables 3 and 4 vs. Table 5), making CEDice outperform the majority of topology loss functions. Although it is unsurprising that data augmentation, self-distillation, and other methods [6] improve performance, limited research has investigated to what extent they can increase topology accuracy, or even if they can make standard models trained on CEDice surpass topology loss functions. Considering that topology loss functions are generally computationally expensive CPU- and GPU-wise (Table 1), our results demonstrate that focusing on improving regular accuracy by utilizing methods that account for dataset challenges can be a resource-friendly alternative to topology loss functions to increase topology accuracy. Moreover, combining such methods with topology loss functions further improved topology accuracy in most cases, especially in the OOD test-set images (Table 5).

TopoMortar was designed to be simple to prevent methods from exploiting dataset particularities to increase topology accuracy. Despite mortar’s relatively simple topology, topology accuracy on TopoMortar has a very high correlation with the topology accuracy on CREMI, DRIVE, FIVES, and CrackTree datasets (Appendix O), demonstrating the **generalizability** of results across biological, non-biological datasets, and structures with different topology.

6. Conclusion

Previous benchmarks on various existing datasets have not allowed to completely understand whether methods improve topology accuracy merely by focusing on the dataset characteristics (thus, disregarding topology), or by incorporating prior topological knowledge. In contrast, our TopoMortar dataset permits to study this research question by eliminating confounding factors and by enabling the investigation of model robustness against various dataset challenges. cIDice generally achieved the most topologically accurate segmentations while Skeleton Recall performed best on noisy labels, which indicates that skeletonization-based topology loss functions have superior topology modeling capabilities.

Acknowledgements. This work was supported by Villum Foundation and NordForsk.

References

- [1] Görkem Algan and Ilkay Ulusoy. Label noise types and their effects on deep learning. *arXiv preprint arXiv:2003.10471*, 2020. 8
- [2] Ricardo J Araújo, Jaime S Cardoso, and Hélder P Oliveira. Topological similarity index and loss function for blood vessel segmentation. *arXiv preprint arXiv:2107.14531*, 2021. 2, 3
- [3] I Arganda-Carreras, HS Seung, A Vishwanathan, and D Berger. 3d segmentation of neurites in em images challenge-isi 2013, 2013. 2, 3
- [4] Ignacio Arganda-Carreras, Srinivas C Turaga, Daniel R Berger, Dan Cireşan, Alessandro Giusti, Luca M Gambardella, Jürgen Schmidhuber, Dmitry Laptev, Sarvesh Dwivedi, Joachim M Buhmann, et al. Crowdsourcing the creation of image segmentation algorithms for connectomics. *Frontiers in neuroanatomy*, 9:152591, 2015. 2, 3
- [5] Favyen Bastani, Songtao He, Sofiane Abbar, Mohammad Alizadeh, Hari Balakrishnan, Sanjay Chawla, Sam Madden, and David DeWitt. Roadtracer: Automatic extraction of road networks from aerial images. In *Proceedings of the IEEE conference on computer vision and pattern recognition*, pages 4720–4728, 2018. 2, 3
- [6] Irwan Bello, William Fedus, Xianzhi Du, Ekin Dogus Cubuk, Aravind Srinivas, Tsung-Yi Lin, Jonathon Shlens, and Barret Zoph. Revisiting resnets: Improved training and scaling strategies. *Advances in Neural Information Processing Systems*, 34:22614–22627, 2021. 8
- [7] Olivier Bernard, Alain Lalonde, Clement Zotti, Frederick Cervenansky, Xin Yang, Pheng-Ann Heng, Irem Cetin, Karim Lekadir, Oscar Camara, Miguel Angel Gonzalez Ballester, et al. Deep learning techniques for automatic mri cardiac multi-structures segmentation and diagnosis: is the problem solved? *IEEE transactions on medical imaging*, 37(11):2514–2525, 2018. 2, 3
- [8] Nick Byrne, James R Clough, Israel Valverde, Giovanni Montana, and Andrew P King. A persistent homology-based topological loss for cnn-based multiclass segmentation of cmr. *IEEE transactions on medical imaging*, 42(1):3–14, 2022. 2, 3
- [9] M Jorge Cardoso, Wenqi Li, Richard Brown, Nic Ma, Eric Kerfoot, Yiheng Wang, Benjamin Murrey, Andriy Myronenko, Can Zhao, Dong Yang, et al. Monai: An open-source framework for deep learning in healthcare. *arXiv preprint arXiv:2211.02701*, 2022. 4
- [10] James R Clough, Ilkay Oksuz, Nicholas Byrne, Julia A Schnabel, and Andrew P King. Explicit topological priors for deep-learning based image segmentation using persistent homology. In *International Conference on Information Processing in Medical Imaging*, pages 16–28. Springer, 2019. 2, 3
- [11] James R Clough, Nicholas Byrne, Ilkay Oksuz, Veronika A Zimmer, Julia A Schnabel, and Andrew P King. A topological loss function for deep-learning based image segmentation using persistent homology. *IEEE transactions on pattern analysis and machine intelligence*, 44(12):8766–8778, 2020. 2, 3
- [12] Ilke Demir, Krzysztof Koperski, David Lindenbaum, Guan Pang, Jing Huang, Saikat Basu, Forest Hughes, Devis Tuia, and Ramesh Raskar. Deepglobe 2018: A challenge to parse the earth through satellite images. In *Proceedings of the IEEE conference on computer vision and pattern recognition workshops*, pages 172–181, 2018. 2, 3
- [13] Lee R Dice. Measures of the amount of ecologic association between species. *Ecology*, 26(3):297–302, 1945. 4
- [14] Edelsbrunner, Letscher, and Zomorodian. Topological persistence and simplification. *Discrete & computational geometry*, 28:511–533, 2002. 4
- [15] Rosana El Jurdi, Caroline Petitjean, Paul Honeine, Veronika Cheplygina, and Fahed Abdallah. High-level prior-based loss functions for medical image segmentation: A survey. *Computer Vision and Image Understanding*, 210:103248, 2021. 2, 6
- [16] Saumya Gupta, Xiaoling Hu, James Kaan, Michael Jin, Mutsipay Mpooy, Katherine Chung, Gagandeep Singh, Mary Saltz, Tahsin Kurc, Joel Saltz, et al. Learning topological interactions for multi-class medical image segmentation. In *European Conference on Computer Vision*, pages 701–718. Springer, 2022. 2
- [17] Saumya Gupta, Yikai Zhang, Xiaoling Hu, Prateek Prasanna, and Chao Chen. Topology-aware uncertainty for image segmentation. *Advances in Neural Information Processing Systems*, 36, 2024. 3
- [18] Hongliang He, Jun Wang, Pengxu Wei, Fan Xu, Xiangyang Ji, Chang Liu, and Jie Chen. Toposeg: Topology-aware nuclear instance segmentation. In *Proceedings of the IEEE/CVF International Conference on Computer Vision*, pages 21307–21316, 2023. 2
- [19] Geoffrey Hinton. Distilling the knowledge in a neural network. *arXiv preprint arXiv:1503.02531*, 2015. 7
- [20] Xiaoling Hu. Structure-aware image segmentation with homotopy warping. *Advances in Neural Information Processing Systems*, 35:24046–24059, 2022. 1, 2, 3, 4
- [21] Xiaoling Hu, Fuxin Li, Dimitris Samaras, and Chao Chen. Topology-preserving deep image segmentation. *Advances in neural information processing systems*, 32, 2019. 1, 3, 4
- [22] Xiaoling Hu, Yusu Wang, Li Fuxin, Dimitris Samaras, and Chao Chen. Topology-aware segmentation using discrete morse theory. *arXiv preprint arXiv:2103.09992*, 2021. 3, 4
- [23] Xiaoling Hu, Dimitris Samaras, and Chao Chen. Learning probabilistic topological representations using discrete morse theory. *arXiv preprint arXiv:2206.01742*, 2022. 2, 3
- [24] Fabian Isensee, Paul F Jaeger, Simon AA Kohl, Jens Petersen, and Klaus H Maier-Hein. nnu-net: a self-configuring method for deep learning-based biomedical image segmentation. *Nature methods*, 18(2):203–211, 2021. 4
- [25] Kai Jin, Xingru Huang, Jingxing Zhou, Yunxiang Li, Yan Yan, Yibao Sun, Qianni Zhang, Yaqi Wang, and Juan Ye.

- Fives: A fundus image dataset for artificial intelligence based vessel segmentation. *Scientific data*, 9(1):475, 2022. 5
- [26] Yannick Kirchhoff, Maximilian R Rokuss, Saikat Roy, Balint Kovacs, Constantin Ulrich, Tassilo Wald, Maximilian Zenk, Philipp Vollmuth, Jens Kleesiek, Fabian Isensee, et al. Skeleton recall loss for connectivity conserving and resource efficient segmentation of thin tubular structures. *arXiv preprint arXiv:2404.03010*, 2024. 2, 3, 4
- [27] Alexander Kirillov, Eric Mintun, Nikhila Ravi, Hanzi Mao, Chloe Rolland, Laura Gustafson, Tete Xiao, Spencer Whitehead, Alexander C Berg, Wan-Yen Lo, et al. Segment anything. In *Proceedings of the IEEE/CVF International Conference on Computer Vision*, pages 4015–4026, 2023. 1
- [28] Xingang Li, Yuebin Wang, Liqiang Zhang, Suhong Liu, Jie Mei, and Yang Li. Topology-enhanced urban road extraction via a geographic feature-enhanced network. *IEEE Transactions on Geoscience and Remote Sensing*, 58(12):8819–8830, 2020. 2
- [29] Wei Liao. Segmentation of tubular structures using iterative training with tailored samples. In *Proceedings of the IEEE/CVF International Conference on Computer Vision*, pages 23643–23652, 2023. 3
- [30] Manxi Lin, Kilian Zepf, Anders Nyman Christensen, Zahra Bashir, Morten Bo Søndergaard Svendsen, Martin Tolsgaard, and Aasa Feragen. Dtu-net: Learning topological similarity for curvilinear structure segmentation. In *International Conference on Information Processing in Medical Imaging*, pages 654–666. Springer, 2023. 2, 3
- [31] Chuni Liu, Boyuan Ma, Xiaojuan Ban, Yujie Xie, Hao Wang, Weihua Xue, Jingchao Ma, and Ke Xu. Enhancing boundary segmentation for topological accuracy with skeleton-based methods. *arXiv preprint arXiv:2404.18539*, 2024. 4
- [32] Sheng Liu, Kangning Liu, Weicheng Zhu, Yiqiu Shen, and Carlos Fernandez-Granda. Adaptive early-learning correction for segmentation from noisy annotations. In *Proceedings of the IEEE/CVF Conference on Computer Vision and Pattern Recognition*, pages 2606–2616, 2022. 5, 1
- [33] Gongning Luo, Kuanquan Wang, Jun Liu, Shuo Li, Xinjie Liang, Xiangyu Li, Shaowei Gan, Wei Wang, Suyu Dong, Wenyi Wang, et al. Efficient automatic segmentation for multi-level pulmonary arteries: The parse challenge. *arXiv preprint arXiv:2304.03708*, 2023. 3
- [34] Leland McInnes, John Healy, and James Melville. Umap: Uniform manifold approximation and projection for dimension reduction. *arXiv preprint arXiv:1802.03426*, 2018. 2
- [35] Volodymyr Mnih. *Machine learning for aerial image labeling*. University of Toronto (Canada), 2013. 2, 1, 3
- [36] Minh Ôn Vũ Ngoc, Nicolas Boutry, and Jonathan Fabrizio. Topology-aware method to segment 3d plan tissue images. In *36th Conference on Neural Information Processing Systems, AI for Science Workshop*, 2022. 2
- [37] Doruk Oner, Mateusz Koziński, Leonardo Citraro, Nathan C Dadap, Alexandra G Konings, and Pascal Fua. Promoting connectivity of network-like structures by enforcing region separation. *IEEE Transactions on Pattern Analysis and Machine Intelligence*, 44(9):5401–5413, 2021. 4, 3
- [38] Doruk Oner, Adélie Garin, Mateusz Koziński, Kathryn Hess, and Pascal Fua. Persistent homology with improved locality information for more effective delineation. *IEEE Transactions on Pattern Analysis and Machine Intelligence*, 45(8):10588–10595, 2023. 2, 3
- [39] Adam Paszke, Sam Gross, Francisco Massa, Adam Lerer, James Bradbury, Gregory Chanan, Trevor Killeen, Zeming Lin, Natalia Gimelshein, Luca Antiga, et al. Pytorch: An imperative style, high-performance deep learning library. *Advances in neural information processing systems*, 32, 2019. 4
- [40] Steffen E Petersen, Paul M Matthews, Jane M Francis, Matthew D Robson, Filip Zemrak, Redha Boubertakh, Al-istair A Young, Sarah Hudson, Peter Weale, Steve Garratt, et al. Uk biobank’s cardiovascular magnetic resonance protocol. *Journal of cardiovascular magnetic resonance*, 18(1):8, 2016. 2, 3
- [41] Yaolei Qi, Yuting He, Xiaoming Qi, Yuan Zhang, and Guanyu Yang. Dynamic snake convolution based on topological geometric constraints for tubular structure segmentation. In *Proceedings of the IEEE/CVF International Conference on Computer Vision*, pages 6070–6079, 2023. 2, 3
- [42] Günter Rote. Computing the minimum hausdorff distance between two point sets on a line under translation. *Information Processing Letters*, 38(3):123–127, 1991. 4
- [43] Pierre Rougé, Nicolas Passat, and Odyssee Merveille. Cascaded multitask u-net using topological loss for vessel segmentation and centerline extraction. *arXiv preprint arXiv:2307.11603*, 2023. 2
- [44] Pengcheng Shi, Jiesi Hu, Yanwu Yang, Zilve Gao, Wei Liu, and Ting Ma. Centerline boundary dice loss for vascular segmentation. *arXiv preprint arXiv:2407.01517*, 2024. 3, 4
- [45] Suprosanna Shit, Johannes C Paetzold, Anjany Sekuboyina, Ivan Ezhov, Alexander Unger, Andrey Zhyhka, Josien PW Pluim, Ulrich Bauer, and Bjoern H Menze. cldice-a novel topology-preserving loss function for tubular structure segmentation. In *Proceedings of the IEEE/CVF conference on computer vision and pattern recognition*, pages 16560–16569, 2021. 1, 3, 4
- [46] Shakir Showkat Sofi and Nadezhda Alshahanova. Image segmentation with topological priors. In *2023 IEEE High Performance Extreme Computing Conference (HPEC)*, pages 1–6. IEEE, 2023. 2, 3
- [47] Joes Staal, Michael D Abràmoff, Meindert Niemeijer, Max A Viergever, and Bram Van Ginneken. Ridge-based vessel segmentation in color images of the retina. *IEEE transactions on medical imaging*, 23(4):501–509, 2004. 2, 5, 3
- [48] Nico Stucki, Johannes C Paetzold, Suprosanna Shit, Bjoern Menze, and Ulrich Bauer. Topologically faithful image segmentation via induced matching of persistence barcodes. In *International Conference on Machine Learning*, pages 32698–32727. PMLR, 2023. 2, 3
- [49] Juan Miguel Valverde and Jussi Tohka. Region-wise loss for biomedical image segmentation. *Pattern Recognition*, 136:109208, 2023. 4
- [50] Heng Wang, Yang Song, Chaoyi Zhang, Jianhui Yu, Siqu Liu, Hanchuan Pengy, and Weidong Cai. Single neuron segmentation using graph-based global reasoning with auxiliary skeleton loss from 3d optical microscope images. In *2021*

- IEEE 18th International Symposium on Biomedical Imaging (ISBI)*, pages 934–938. IEEE, 2021. [2](#)
- [51] Haotian Wang, Min Xian, and Aleksandar Vakanski. Ta-net: Topology-aware network for gland segmentation. In *Proceedings of the IEEE/CVF winter conference on applications of computer vision*, pages 1556–1564, 2022. [2](#)
- [52] Liwei Wang, Chen-Yu Lee, Zhuowen Tu, and Svetlana Lazebnik. Training deeper convolutional networks with deep supervision. *arXiv preprint arXiv:1505.02496*, 2015. [2](#)
- [53] Yan Wang, Xu Wei, Fengze Liu, Jieneng Chen, Yuyin Zhou, Wei Shen, Elliot K Fishman, and Alan L Yuille. Deep distance transform for tubular structure segmentation in ct scans. In *Proceedings of the IEEE/CVF Conference on Computer Vision and Pattern Recognition*, pages 3833–3842, 2020. [2](#)
- [54] Jiaqi Yang, Xiaoling Hu, Chao Chen, and Chialing Tsai. A topology-attention convlstm network and its application to em images. *arXiv preprint arXiv:2202.03430*, 2022. [2](#), [3](#)
- [55] Kaiyuan Yang, Fabio Musio, Yihui Ma, Norman Juchler, Johannes C Paetzold, Rami Al-Maskari, Luciano Höher, Hongwei Bran Li, Ibrahim Ethem Hamamci, Anjany Sekuboyina, et al. Benchmarking the cow with the topcow challenge: Topology-aware anatomical segmentation of the circle of willis for cta and mra. *ArXiv*, 2023. [3](#)
- [56] Qin Zou, Yu Cao, Qingquan Li, Qingzhou Mao, and Song Wang. Cracktree: Automatic crack detection from pavement images. *Pattern Recognition Letters*, 33(3):227–238, 2012. [2](#), [5](#), [3](#)

TopoMortar: A dataset to evaluate image segmentation methods focused on topology accuracy

Supplementary Material

A. Massachusetts Roads corrupted images

The Massachusetts Roads dataset²³ [35]—one of the most popular datasets for evaluating topology loss functions—contains several images with large white patches that occlude the aerial images but not their ground truth. Specifically, we counted 320 images in the training set (around one third of the total) that have over 10% white pixels (*i.e.*, [255, 255, 255]), indicating that they are corrupted. Figure 1 shows two representative examples. This issue, and whether it has been tackled and how, has been largely unreported.

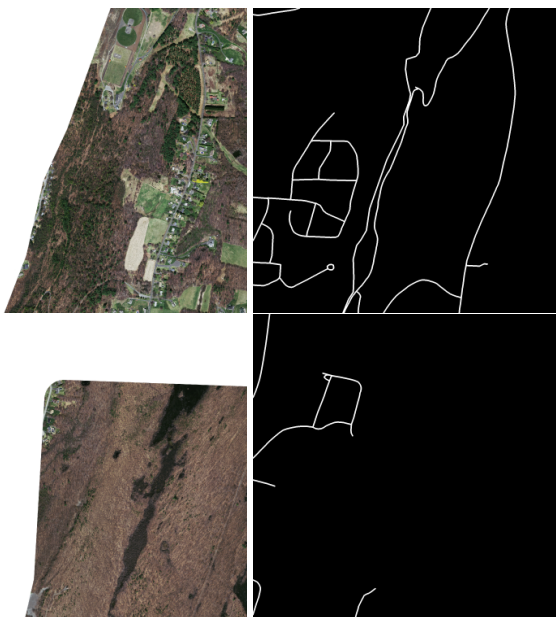


Figure 1. Two of the 320 corrupted images (left) with their ground truth (right).

B. CREMI dataset

CREMI dataset is originally composed by three electron-microscopy images of the brain tissue of adult *Drosophila melanogaster* and the instance segmentation of the axons (see Figure 2 (top)). Previous studies focusing on topology loss functions have utilized this instance segmentation to derive pseudo-labels of the axon borders. This process have not been exhaustively documented, and, as we

²<https://www.cs.toronto.edu/~vmnih/data/>

³<https://www.kaggle.com/datasets/balraj98/massachusetts-roads-dataset>

report here, utilizing different thresholds on the distance maps can lead to pseudo-labels with very different size and topology. For instance, applying a threshold value of “4” (Figure 2 bottom-right) increases by 33% the size of the pseudo-labels compared to a threshold value of “3” (Figure 2 bottom-left), while the small cycles (Figure 2 top-right dark blue) tend to disappear, thus, changing its topology.

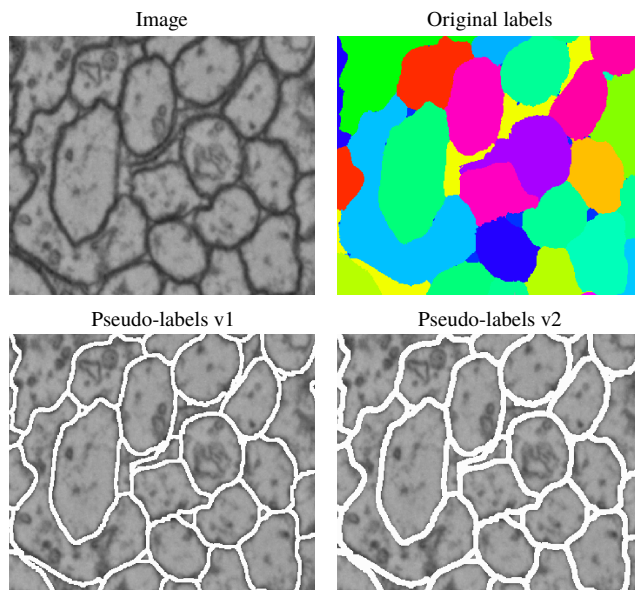


Figure 2. (a) Representative crop of CREMI dataset, (b) its ground-truth labels, and (c-d) two pseudo-labels derived with distance transform applying different thresholds.

C. CrackTree segmentation example

Figure 3 illustrates an example of CrackTree dataset, its corresponding annotation that is a line of only one-pixel width, and the segmentation with standard supervised learning and Adele [32].

D. Datasets used to evaluate topology loss functions

Table 1 lists the datasets used by, at least, two of the 28 recent studies that we examined that proposed a topology-focused image segmentation method. Table 1 also shows the training and optimization settings of these works, where we can observe a large discrepancy across experiments in previous works. In addition to these datasets, 35 other datasets were used by only one study.

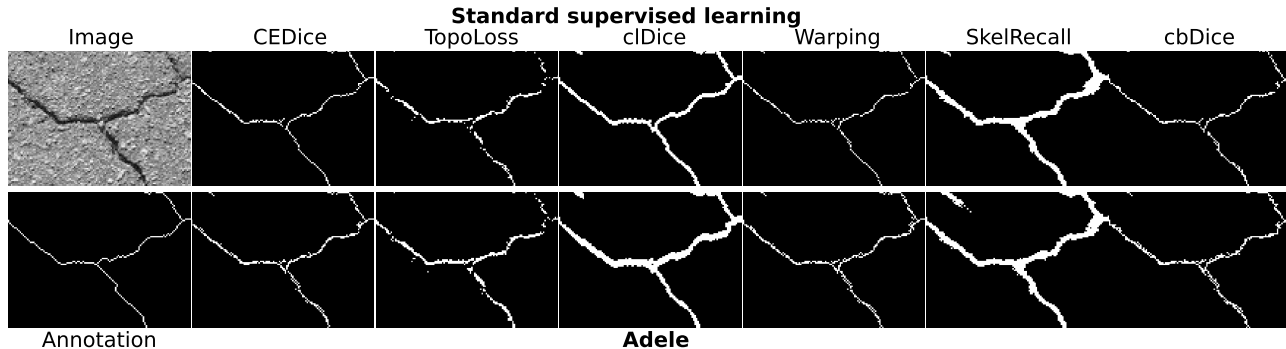


Figure 3. Representative segmentations in CrackTree. Top: Loss functions trained via standard supervised learning. Bottom: Trained via Adele.

E. TopoMortar’s dataset split

We generated the training, validation and test-set split automatically, maximizing the diversity of the images. We manually cropped 823 512×512 patches from the original photographs that we, afterwards, classified into in-distribution and the six out-of-distribution categories (shadows, graffiti, colors, angles, objects, occlusion). For the purpose of creating the dataset split, we down-scaled the patches to 256×256 , flatten them, and, for each patch, we computed the histogram (1000 bins) of its intensity values, resulting into 823 1000-length vectors. We then grouped the vectors by their category and reduced their dimensionality to two components with UMAP [34]. We divided the embedded space into a 5×5 grid, and we uniformly sampled the images from the cells, achieving the desired number of images per category: 120 images for in-distribution, and 50 for each of the six out-of-distribution groups. Figure 4 illustrates this process. Finally, we randomly divided the in-distribution group into 50-20-50 for the training, validation, and test set, and included all the out-of-distribution images in the test set.

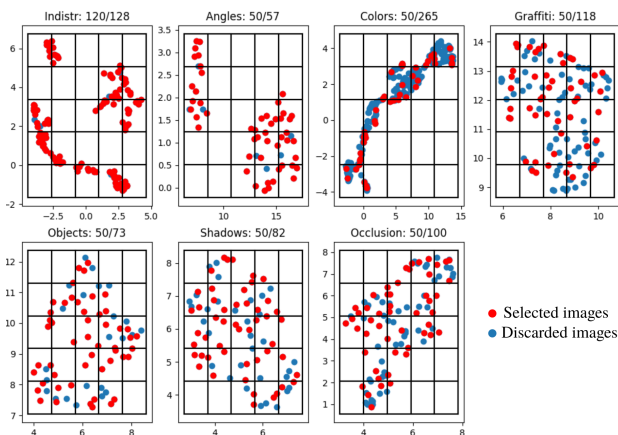


Figure 4. UMAP embeddings of TopoMortar’s cropped patches separated by category.

F. Examples of occlusion

Figure 5 illustrates examples where structures are occluded by objects and that topology-aware methods should, ideally, be able to handle.

G. Optimization details

We trained nnUNet for 12,000 iterations on batches of 10 images with deep supervision [52] and stochastic gradient descent, with a learning rate of 0.01, nesterov momentum of 0.99, weight decay of 3×10^{-5} , and polynomial learning rate decay $(1 - \frac{iteration}{12000})^{0.9}$. Each experimental setting was run with 10 different random seeds, and we employed 10 data augmentation transformations (see Table 2).

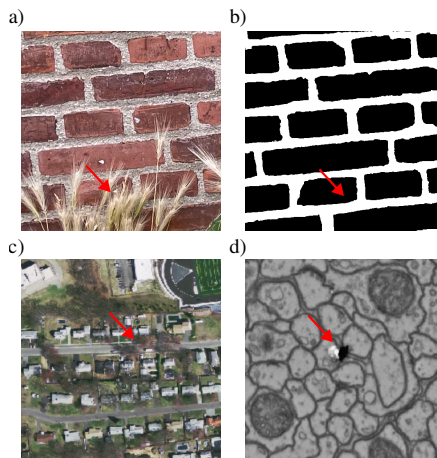


Figure 5. Structures that appear disconnected due to occlusion. a-b) TopoMortar’s “occlusion” image and its ground truth. c) Massachusetts Roads’ image with trees occluding the road. d) CREMI crop with debris occluding the myelin.

Dataset	Information	Training configuration	Architecture	Runs	D.A.	Study
DRIVE [47]	- 40 2D images - Blood vessels - Optical coherence tomography	5-fold xval on 20 images	nnUNet, HRNet	?	?	[26]
		3-fold xval on 30 images	UNet, FCN	?	?	[45]
		Unspecified split on 20 images	UNet	?	?	[20]
		3-fold xval on 20 images	?	?	?	[21]
		16-4-20 train-val-test	nnUNet	?	✓	[44]
		16-4-20 train-val-test	UNet	?	?	[17]
		3-fold xval	ProbabilisticUnet	?	?	[23]
		16-4 train-test	UNet	?	?	[30]
		3-fold xval on 20 images	UNet	?	?	[22]
		16-4-20 train-val-test	UNet	2	✓	[2]
Massachusetts Roads [35]	- 1171 2D images - Roads - Satellite imagery	Unspecified split on 20 images	DSCNet	?	✓	[41]
		20-20 train-test	Own method	?	✓	[29]
		Predefined split on 804 images	nnUNet, HRNet	?	?	[26]
		3-fold xval on 120 images	UNet, custom FCN	?	?	[45]
		3-fold xval	UNet	?	?	[20]
		3-fold xval on 1108 images	?	?	?	[21]
		100-24 train-test	UNet	?	?	[48]
		3-fold xval	UNet	?	✓	[37]
		1108-14-49 train-val-test	UNet	?	?	[17]
		3-fold xval on 1108 images	UNet	?	?	[22]
CREMI ⁴	- 3 3D images - Neuron borders - Electron microscopy	3-fold xval on 324 slices	UNet	?	?	[45]
		3-fold xval	UNet	?	?	[20]
		3-fold xval on 125 slices	Unspecified	?	?	[21]
		100-25 slices (train-test)	UNet	?	?	[48]
		3-fold xval on 125 slices	ProbabilisticUnet	?	?	[23]
		3-fold xval on 125 slices	UNet	?	?	[22]
		3-fold xval	ConvLSTM	?	✓	[54]
ISBI12 [4]	- 30 2D slices - Neuron borders - Electron microscopy	3-fold xval	?	?	?	[21]
		3-fold xval	UNet	?	?	[22]
		3-fold xval	ConvLSTM	?	✓	[54]
		24-6 train-test	UNet	?	✓	[46]
ISBI13 [3]	- 100 2D slices - Neuron borders - Electron microscopy	3-fold xval	?	?	?	[21]
		3-fold xval	ProbabilisticUnet	?	?	[23]
		3-fold xval	UNet	?	?	[22]
		3-fold xval	ConvLSTM	?	✓	[54]
RoadTracer [5]	- 300 2D images of 40 cities - Roads - Satellite imagery	180-120 train-val	UNet	?	?	[20]
		25-15 cities train-val	UNet	?	✓	[37]
		25-15 cities train-val	UNet	1	✓	[38]
CrackTree [56]	- 206 2D images - Concrete cracks - Photographs	3-fold xval	?	?	?	[21]
		3-fold xval	UNet	?	?	[22]
DeepGlobe [12]	- 8570 2D images - Roads - Satellite imagery	4696-1530 train-val	UNet	?	?	[20]
		4696-1530 train-val	UNet	?	✓	[37]
TopCow [55]	- 110+90 3D images - Circle of Willis - 110 MRI, 90 CTA	Predefined train-test	nnUNet, HRNet	?	?	[26]
		72-18 (CTA) train-val	nnUNet	?	✓	[44]
Parse2022 [33]	- 100 3D images - Pulmonary arteries - CT	80-20 train-test	nnUNet	?	✓	[44]
		4-fold xval	UNet	?	?	[17]
Left ventricle UK Biobank [40]	- 900 images - Ventricles - Cardiac MRI	Various settings	UNet	20	?	[10]
		Various settings	UNet	?	?	[11]
ACDC [7]	- 150 patients (4D) - Ventricles, Myocardium - Cardiac MRI	100-50 train-test	UNet	?	?	[11]
		300-150-150 (slices) train-val-test	UNet	?	✓	[8]

Table 1. Datasets and experimental setting across studies on topology and image segmentation. Information: **Number of images**, target region of interest, and imaging modality. Runs: Number of independent runs with different random seeds. D.A.: Data augmentation. ?: Unspecified.

Transformation (probability)	Parameters
Rand. rotation (0.2)	$[-\pi, \pi]$
Rand. scale (0.2)	$[0.7, 1.4]$
Gaussian noise (0.1)	$N(0, 0.1)$
Gaussian blur (0.2)	$\sigma_x=[0.5, 1], \sigma_y=[0.5, 1]$
Rand. intensity scale (0.15)	$[-0.25, 0.25]$
Rand. intensity scale (fixed mean) (0.15)	$[-0.25, 0.25]$
Rand. low resolution (0.25)	$[0.5, 1]$
Rand. adjust contrast (inverted image) (0.1)	$[0.7, 1.5]$
Rand. adjust contrast (0.1)	$[0.7, 1.5]$
Rand. axis flip (0.5)	-

Table 2. Data augmentation used in all our experiments.

G.1. Loss functions configuration and hyper-parameters

We employed eight loss functions, including the combination of Cross entropy and Dice loss, and the seven loss functions described below. In our experiments, we utilized the official Github source code of those seven loss functions.

RegionWise loss In the original study [49], the region-wise maps \mathbf{z} corresponded to the distance to the border of the ground truth. Since, in the second and third self-distillation iterations, the pseudo-labels are softmax probabilities, we computed region-wise loss differently. We considered the softmax probabilities as if they were distances, and the probabilities > 0.9 were considered to indicate the presence of the foreground.

TopoLoss In agreement with the original study [21], we combined TopoLoss with Cross entropy loss (*i.e.*, $\mathcal{L} = \mathcal{L}_{ce} + \lambda\mathcal{L}_{warp}$). Due to the long time required to compute TopoLoss, we set $\lambda = 0$ during the first 70% of the training time, and $\lambda = 100$ during the remaining 30%. Additionally, we set $path_size = 50$.

TOPO In agreement with the original study [37], we combined TOPO windowed loss with Mean square error loss (*i.e.*, $\mathcal{L} = \mathcal{L}_{MSE} + \alpha\mathcal{L}_{TOPO}$). We set $\alpha = 0.001$. Additionally, since models trained with TOPO windowed loss produced outputs of only one channel, in the self-distillation experiments pseudo-labels were binarized.

clDice loss In agreement with the original study [45], we combined clDice loss with Dice loss (*i.e.*, $\mathcal{L} = (1 - \alpha)(1 - \mathcal{L}_{dice}) + \alpha(1 - \mathcal{L}_{clDice})$). The hyper-parameters that we used were: $\alpha = 0.5, k = 3$ (number of iterations).

Warping loss In agreement with the original study [20], we combined Warping loss with Dice loss (*i.e.*, $\mathcal{L} = \mathcal{L}_{dice} + \lambda\mathcal{L}_{warp}$). Due to the long time required to compute Warping loss, we set $\lambda = 0$ during the first 70% of the training time, and $\lambda = 0.1$ during the remaining 30%.

Skeleton Recall loss In agreement with the original study [26], we combined Skeleton Recall loss with Cross entropy loss (*i.e.*, $\mathcal{L} = \mathcal{L}_{ce} + \lambda\mathcal{L}_{skel_recall}$). We set $\lambda = 1$.

cbDice loss In agreement with the original study [44], we combined Centerline boundary Dice loss with Cross entropy and Dice loss (*i.e.*, $\mathcal{L} = 0.5\mathcal{L}_{ce} + \frac{\alpha}{2(\alpha+\beta)}\mathcal{L}_{dice} + \frac{\beta}{2(\alpha+\beta)}\mathcal{L}_{cbDice}$). We set $\alpha = \beta = 1$.

H. CREMI segmentation results

In CREMI, 1-dimensional topological structures (*i.e.*, holes, cycles) correspond to axons. However, the β_1 error, which is the difference in the number of holes between the ground truth and the automatic prediction, cannot distinguish between correct and incorrect holes. Since applying no data augmentation leads to inaccurate segmentations with more incorrect holes in the borders and CREMI’s pseudo-labels contain numerous holes, it appears that the lack of data augmentation leads to topologically more correct segmentations. In other words, segmentations with more wrong holes often achieved smaller β_1 errors (Figure 6), making CREMI unsuitable to measure β_1 errors.

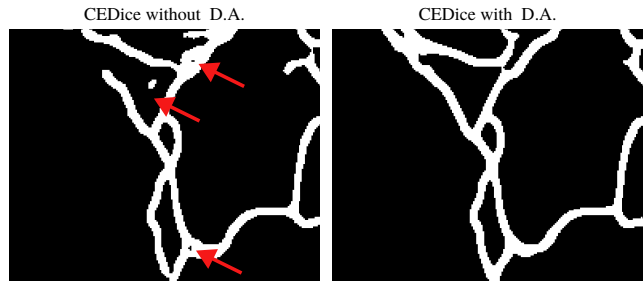


Figure 6. A slice of CREMI dataset segmented by CEDice with and without data augmentation. Left: The lack of data augmentation led to more holes, but also to more wrong openings. Right: Data augmentation helped in achieving more realistic segmentations.

I. Any loss can be made appear the best

We observed that the majority of previous works did not report the use of more than one random seed—possibly due to the large computational requirements associated to topological loss functions. In this study, where we run every experiment with 10 random seeds, we noticed that the large variability in the Betti errors permits to portray almost any loss function as the most topologically accurate by carefully selecting a random seed. Figure 7 illustrates this issue in CREMI dataset (with data augmentation): to make any loss appear the best, one would need to select the random seed corresponding to the green circle, and for the others the random seed corresponding to the orange circle.

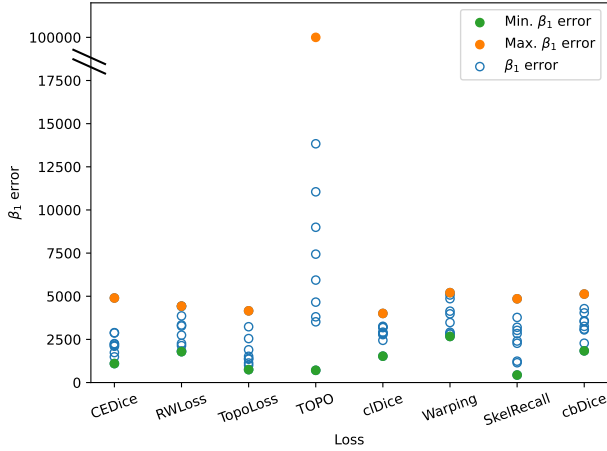


Figure 7. β_1 errors for each loss function in CREMI dataset (with data augmentation). Green: Smallest β_1 error. Orange: Largest β_1 error. Blue: Others.

J. Segmentations on TopoMortar’s OOD test set

Figure 8 shows images and their corresponding labels, categorized by their out-of-distribution group, and the segmentations achieved by training on each loss function.

K. Significance tests

P-values were obtained by the paired permutation test comparing the Betti errors between methods. We considered results with $p < 0.05$ to be statistically significant.

- Figure 9: p-values corresponding to Section 4.1 “Challenges and limitations in previous datasets” (Table 2).
- Figure 10: p-values corresponding to Section 4.2 “Benchmark on TopoMortar without challenges” (Table 3).
- Figure 11: p-values corresponding to Section 4.3 “Robustness to scarce training data, low-quality labels, and OOD images” (Table 4).
- Figure 12: p-values corresponding to Section 4.4 “Topology losses with data augmentation and self-distillation” (Table 5).

L. Dice and HD95 measurements

Tables 3 and 4 show the Dice coefficients and HD95 from Section 4.3 “Robustness to scarce training data, low-quality labels, and OOD images” and Section 4.4 “Topology losses with data augmentation and self-distillation”, respectively.

M. RandHue data augmentation

Figure 13 illustrates representative examples of TopoMortar training images augmented with *RandHue*.

Test set →	Dice		HD95		
	ID	OOD	ID	OOD	
Small training set	CEDice	0.9 ± 0.0	0.55 ± 0.0	2.06 ± 0.11	39.57 ± 1.11
	RWLoss	0.9 ± 0.0	0.57 ± 0.01	2.04 ± 0.06	39.46 ± 1.35
	TopoLoss	0.9 ± 0.0	0.56 ± 0.01	2.09 ± 0.11	39.86 ± 1.17
	TOPO	0.86 ± 0.0	0.59 ± 0.01	2.64 ± 0.22	40.54 ± 0.58
	cDice	0.9 ± 0.0	0.56 ± 0.01	2.04 ± 0.09	39.83 ± 1.88
	Warping	0.9 ± 0.0	0.56 ± 0.01	2.06 ± 0.07	39.56 ± 1.26
	SkelRecall	0.9 ± 0.0	0.57 ± 0.01	2.1 ± 0.12	39.68 ± 0.86
	cbDice	0.9 ± 0.0	0.56 ± 0.01	2.08 ± 0.11	39.62 ± 0.92
Pseudo-labels	CEDice	0.86 ± 0.0	0.68 ± 0.01	3.17 ± 0.02	35.19 ± 2.6
	RWLoss	0.87 ± 0.0	0.67 ± 0.01	3.09 ± 0.03	36.65 ± 1.12
	TopoLoss	0.86 ± 0.0	0.68 ± 0.01	3.18 ± 0.02	36.33 ± 2.51
	TOPO	0.81 ± 0.0	0.66 ± 0.01	4.4 ± 0.06	40.53 ± 0.81
	cDice	0.87 ± 0.0	0.67 ± 0.01	3.17 ± 0.02	36.87 ± 0.88
	Warping	0.87 ± 0.0	0.67 ± 0.01	3.12 ± 0.03	36.43 ± 1.29
	SkelRecall	0.86 ± 0.0	0.7 ± 0.01	3.29 ± 0.03	34.91 ± 1.37
	cbDice	0.86 ± 0.0	0.68 ± 0.01	3.13 ± 0.02	35.72 ± 2.52
Noisy labels	CEDice	0.63 ± 0.0	0.33 ± 0.01	3.84 ± 0.02	40.17 ± 2.02
	RWLoss	0.66 ± 0.0	0.31 ± 0.01	3.57 ± 0.01	36.35 ± 1.51
	TopoLoss	0.62 ± 0.0	0.26 ± 0.01	3.88 ± 0.02	42.99 ± 2.81
	TOPO	0.84 ± 0.01	0.58 ± 0.01	2.65 ± 0.19	39.27 ± 0.84
	cDice	0.69 ± 0.0	0.46 ± 0.01	3.58 ± 0.01	38.9 ± 1.46
	Warping	0.62 ± 0.0	0.35 ± 0.0	3.85 ± 0.01	37.61 ± 0.98
	SkelRecall	0.76 ± 0.0	0.51 ± 0.01	3.24 ± 0.01	40.16 ± 1.8
	cbDice	0.63 ± 0.0	0.31 ± 0.01	3.82 ± 0.01	39.26 ± 2.18

Table 3. Dice and HD95 measurements complementary to Table 4 in Section 4.3 “Robustness to scarce training data, low-quality labels, and OOD images”.

Test set →	Dice		HD95		
	ID	OOD	ID	OOD	
D.A. (RandHue)	CEDice	0.91 ± 0.0	0.74 ± 0.01	1.88 ± 0.31	36.1 ± 0.68
	RWLoss	0.91 ± 0.0	0.72 ± 0.01	1.8 ± 0.01	36.54 ± 0.54
	TopoLoss	0.91 ± 0.0	0.74 ± 0.01	1.9 ± 0.52	36.19 ± 0.52
	TOPO	0.86 ± 0.0	0.72 ± 0.01	2.64 ± 0.49	42.31 ± 1.06
	cDice	0.91 ± 0.0	0.74 ± 0.01	1.77 ± 0.0	35.42 ± 0.69
	Warping	0.91 ± 0.0	0.73 ± 0.01	1.8 ± 0.05	35.94 ± 0.73
	SkelRecall	0.91 ± 0.0	0.75 ± 0.01	1.91 ± 0.28	37.83 ± 0.72
	cbDice	0.91 ± 0.0	0.74 ± 0.01	1.89 ± 0.48	36.5 ± 0.78
Pseudo + Self. dist.	CEDice	0.87 ± 0.0	0.69 ± 0.01	3.11 ± 0.04	36.34 ± 2.24
	RWLoss	0.87 ± 0.0	0.67 ± 0.01	3.11 ± 0.03	36.09 ± 1.04
	TopoLoss	0.86 ± 0.0	0.68 ± 0.01	3.43 ± 0.03	37.93 ± 2.66
	TOPO	0.76 ± 0.0	0.63 ± 0.01	5.56 ± 0.37	39.74 ± 0.97
	cDice	0.88 ± 0.0	0.63 ± 0.01	3.24 ± 0.08	37.82 ± 0.56
	Warping	0.88 ± 0.0	0.66 ± 0.01	3.01 ± 0.03	36.48 ± 1.48
	SkelRecall	0.86 ± 0.0	0.68 ± 0.01	3.4 ± 0.05	36.44 ± 1.26
	cbDice	0.87 ± 0.0	0.68 ± 0.01	3.06 ± 0.05	37.29 ± 2.19
Noisy + Self. dist.	CEDice	0.65 ± 0.0	0.35 ± 0.01	3.72 ± 0.02	42.12 ± 2.15
	RWLoss	0.66 ± 0.0	0.3 ± 0.01	3.62 ± 0.11	36.97 ± 1.81
	TopoLoss	0.6 ± 0.01	0.25 ± 0.01	4.09 ± 1.08	71.88 ± 44.92
	TOPO	0.83 ± 0.02	0.54 ± 0.02	3.52 ± 0.85	41.72 ± 1.06
	cDice	0.78 ± 0.0	0.49 ± 0.01	2.98 ± 0.01	42.41 ± 3.58
	Warping	0.67 ± 0.0	0.37 ± 0.0	3.56 ± 0.02	42.07 ± 2.47
	SkelRecall	0.79 ± 0.0	0.55 ± 0.01	3.08 ± 0.02	39.94 ± 2.0
	cbDice	0.69 ± 0.0	0.35 ± 0.0	3.44 ± 0.02	42.83 ± 1.75

Table 4. Dice and HD95 measurements complementary to Table 5 in Section 4.4 “Topology losses with data augmentation and self-distillation”.

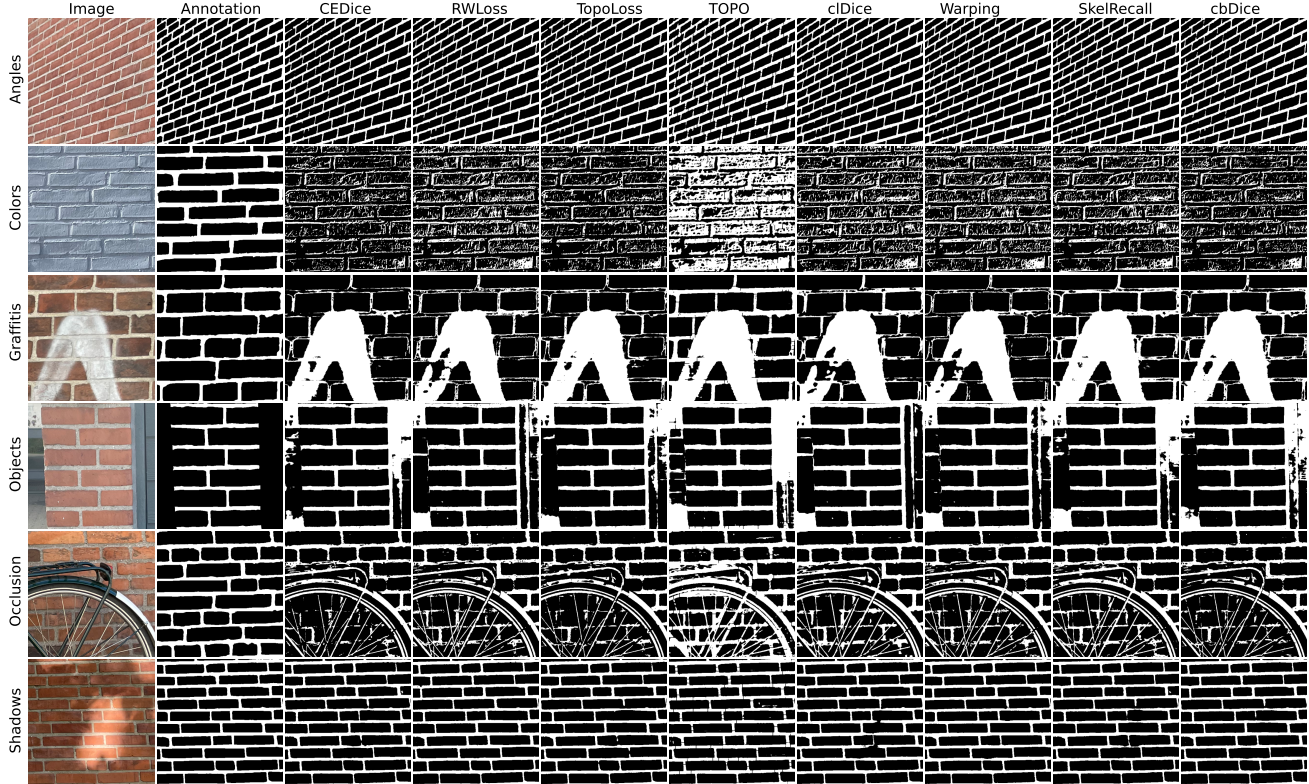


Figure 8. Segmentations with median performance obtained on the following training setup: Standard supervised learning, large training set, accurate labels.

	OOD group	β_0 error	β_1 error	Dice	HD95
Baseline	Angles	56.36 \pm 19.77	27.74 \pm 18.99	0.87 \pm 0.01	5.19 \pm 1.04
	Colors	605.0 \pm 66.74	257.8 \pm 45.09	0.5 \pm 0.01	10.65 \pm 0.31
	Graffiti	135.37 \pm 19.9	70.49 \pm 19.2	0.53 \pm 0.0	34.04 \pm 1.89
	Objects	118.13 \pm 33.13	74.11 \pm 27.15	0.42 \pm 0.01	144.19 \pm 1.59
	Occlusion	87.07 \pm 7.32	70.03 \pm 10.57	0.76 \pm 0.0	24.39 \pm 0.63
	Shadows	68.44 \pm 16.89	35.85 \pm 15.53	0.83 \pm 0.01	8.62 \pm 1.34
RandHue	Angles	34.69 \pm 9.29	17.92 \pm 5.8	0.86 \pm 0.01	5.84 \pm 0.37
	Colors	77.25 \pm 12.71	47.12 \pm 8.44	0.79 \pm 0.01	5.42 \pm 0.3
	Graffiti	95.24 \pm 10.78	80.97 \pm 11.27	0.6 \pm 0.01	31.46 \pm 0.71
	Objects	87.99 \pm 12.69	75.34 \pm 13.45	0.53 \pm 0.01	145.83 \pm 1.66
	Occlusion	74.1 \pm 7.91	73.46 \pm 8.74	0.78 \pm 0.0	23.98 \pm 0.26
	Shadows	38.96 \pm 12.33	30.86 \pm 10.42	0.85 \pm 0.01	10.08 \pm 0.98

Table 5. Average measurements across loss functions per OOD group. Baseline: Corresponding to Section 4.2 “Benchmark on TopoMortar without challenges” (Table 3). RandHue: Corresponding to Section 4.4 “Topology losses with data augmentation and self-distillation” (Table 5, RandHue)

N. Baseline and RandHue results divided by OOD groups

Table 5 shows the average β_0 , β_1 , Dice coefficient and HD95 across the different loss functions on the OOD test set, separating the measurements by OOD group.

O. High correlation between topology accuracy on TopoMortar and other datasets

TopoMortar is designed as a dataset that permits to control for dataset task confounding variables by fixing a task (segmenting mortar in red brick wall images) in order to study the individual effect on topology accuracy of four dataset challenges: small training set, noisy labels, pseudo-labels, and OOD test-set images. This, ultimately, allows to elucidate the context in which topology-focused image segmentation methods, such as topology loss functions, are advantageous. Importantly, although TopoMortar task is on mortar segmentation, our results are extrapolable to other datasets, which demonstrates the **generalizability of our conclusions** to biology and non-biology datasets.

Table 6 shows the Pearson correlation between the topology accuracy obtained by topology loss functions in TopoMortar and the topology accuracy obtained in CREMI, DRIVE, FIVES, and CrackTree datasets. The high correlations demonstrate 1) that TopoMortar can represent dataset challenges (Table 6, first three rows), and 2) that TopoMortar can represent the results obtained after tackling dataset challenges (Table 6, last two rows).

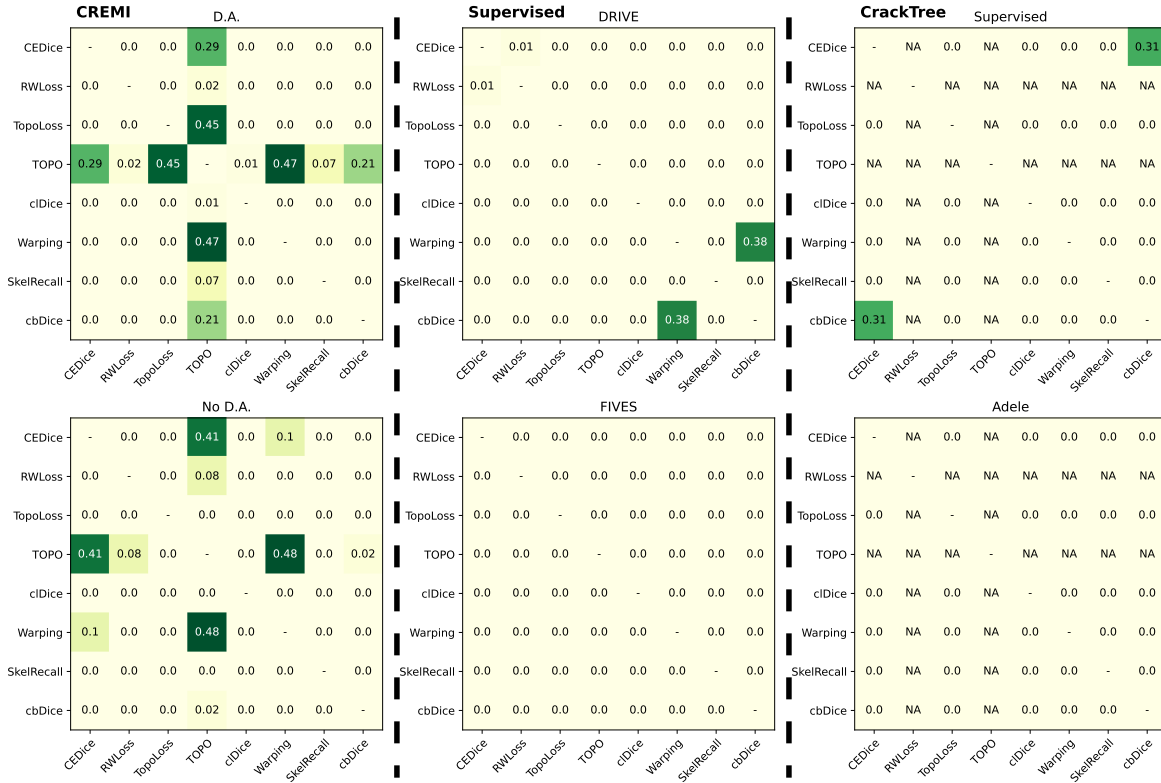


Figure 9. P-values corresponding to Table 2 in Section 4.1 “Challenges and limitations in previous datasets”. Training setup: (Left column) CREMI with and without DA, (middle column) DRIVE vs. FIVES datasets, (right column) CrackTree via standard supervised learning vs. via Adele.

Setting 1	Setting 2	Corr.
CREMI, Data augmentation, β_1	TopoMortar, Pseudo labels, In distribution, β_1	0.933
DRIVE, β_0	TopoMortar, Small training set, In distribution, β_0	0.905
CrackTree, Supervised, β_0	TopoMortar, Noisy labels, In distribution, β_0	0.643
FIVES, β_0	TopoMortar, Large training set, In distribution, β_0	0.782
CrackTree, Adele, β_0	TopoMortar, Noisy labels, Self-distillation, β_0	0.920

Table 6. Pearson correlation between experimental settings using existing datasets and their corresponding representation in TopoMortar.

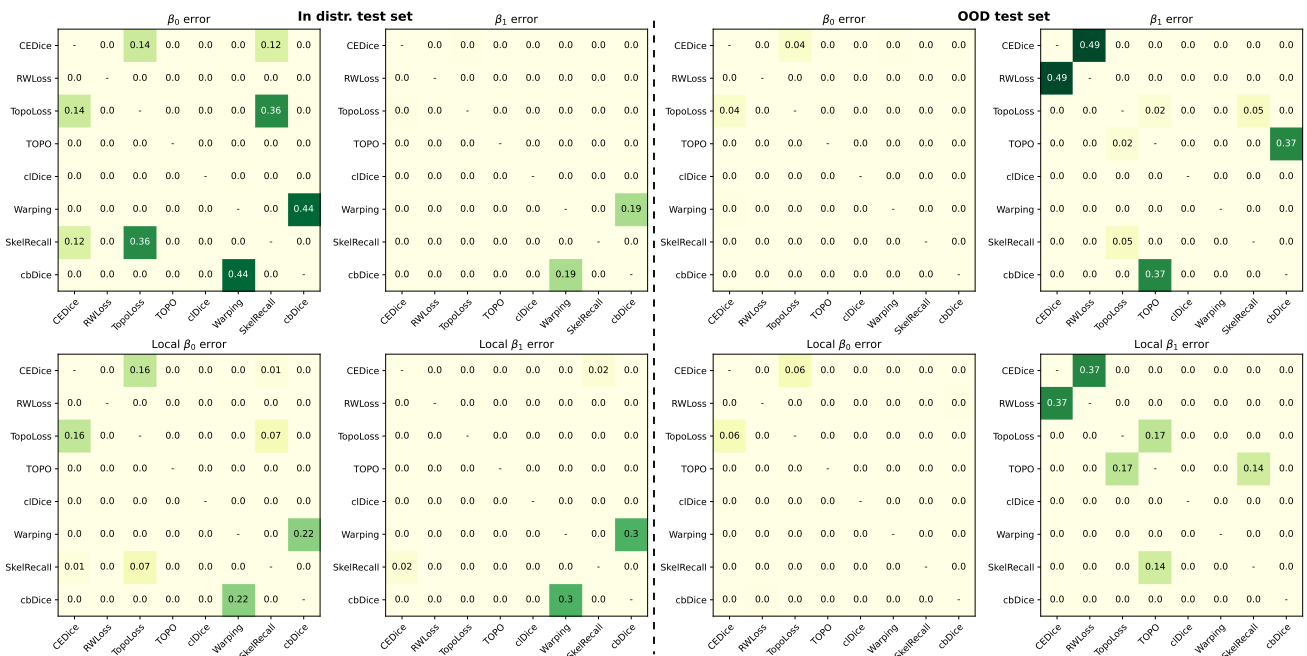


Figure 10. P-values corresponding to Table 3 in Section 4.2 “Benchmark on TopoMortar without challenges”. Training setup: TopoMortar, standard supervised learning, large training set, accurate labels.

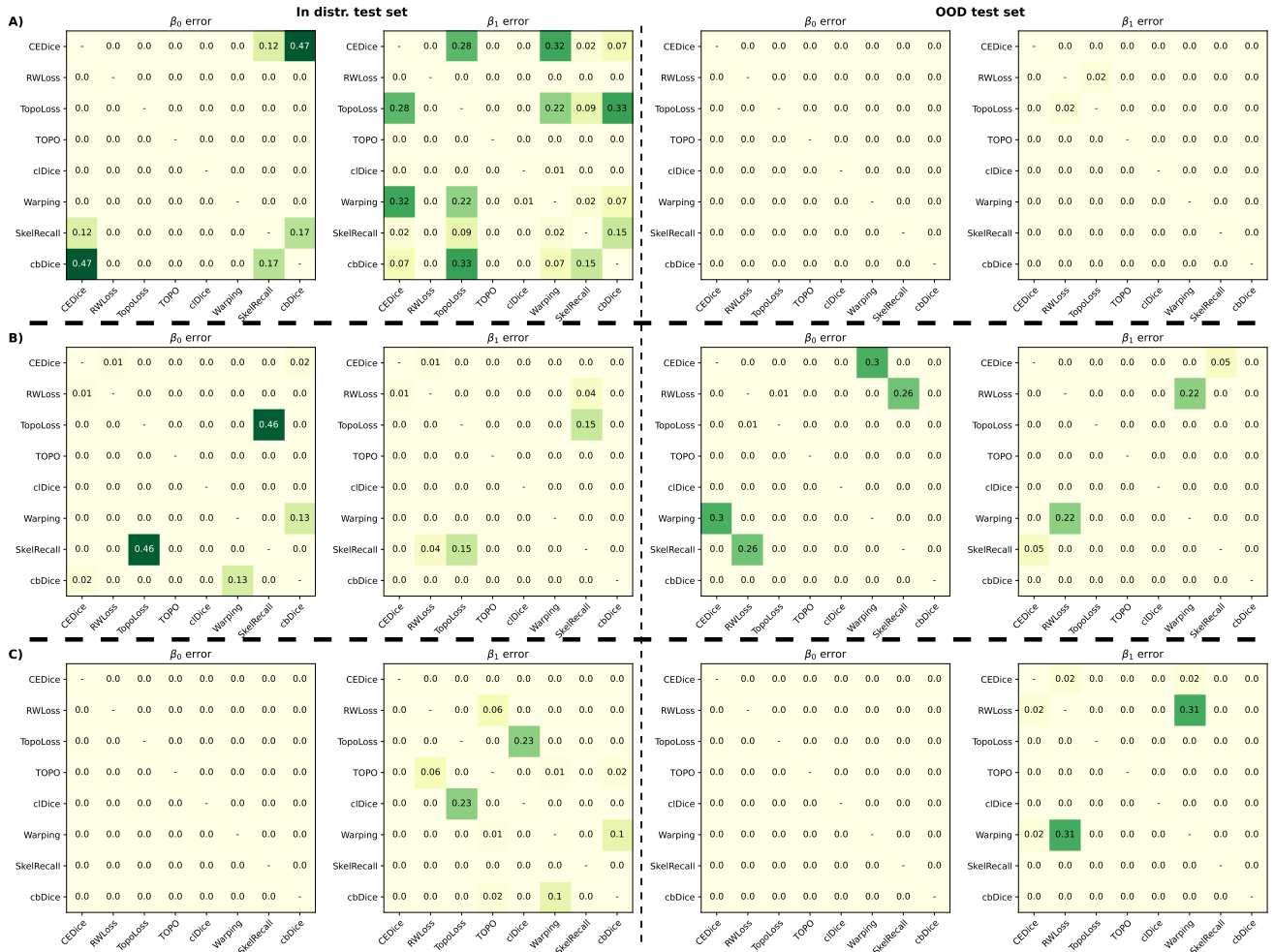


Figure 11. P-values corresponding to Table 4 in Section 4.3 “Robustness to scarce training data, low-quality labels, and OOD images”. A: Standard supervised learning, *small training set*, accurate labels. B: Standard supervised, large training set, *pseudo-labels*. C: Standard supervised learning, large training set, *noisy labels*.

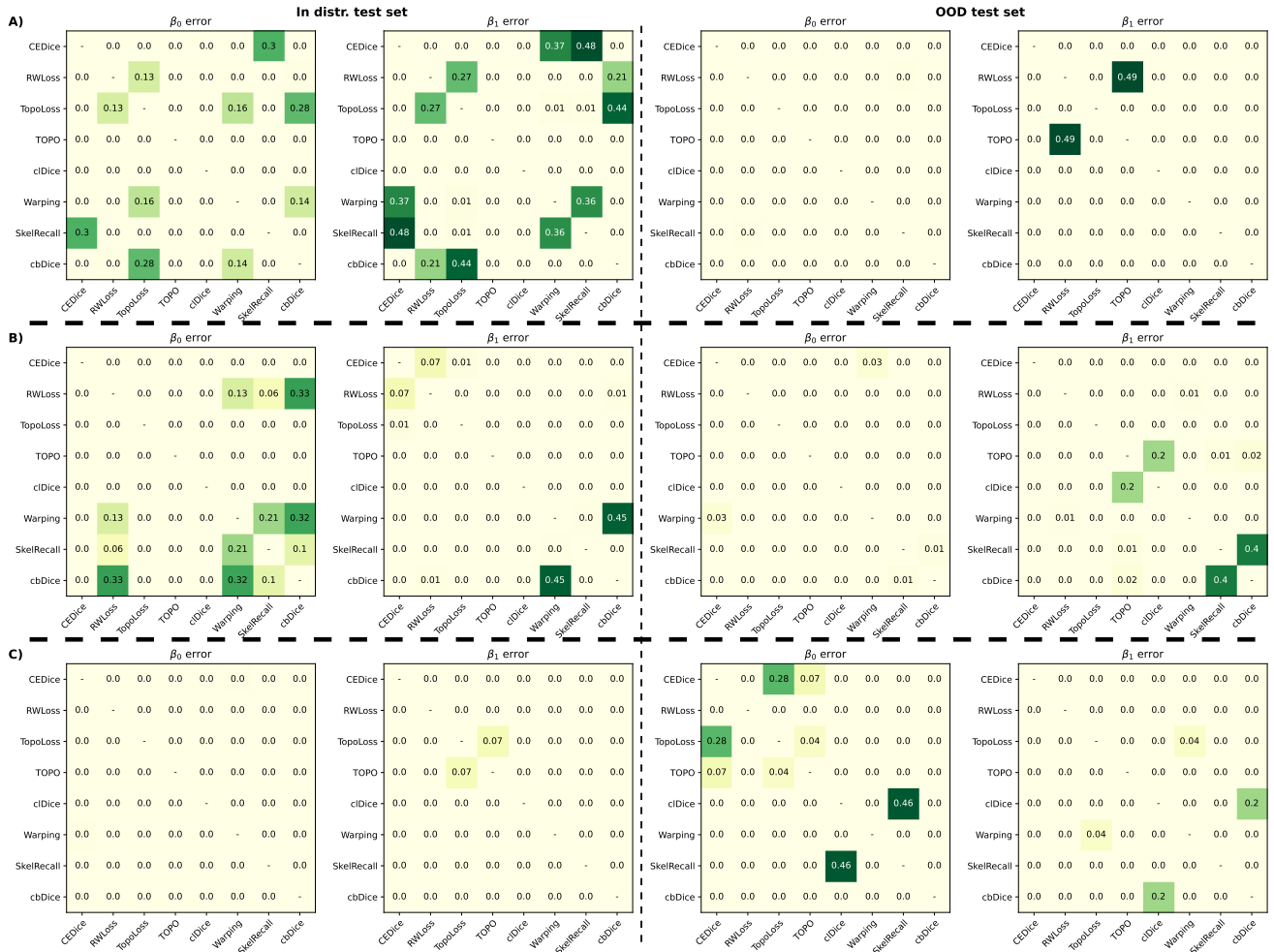


Figure 12. P-values corresponding to Table 5 in Section 4.4 “Topology losses with data augmentation and self-distillation”. A: Standard supervised learning, small training set, accurate labels, with the extra data augmentation *RandHue*. B: *Self-distillation*, large training set, pseudo-labels. C: *Self-distillation*, large training set, noisy labels.

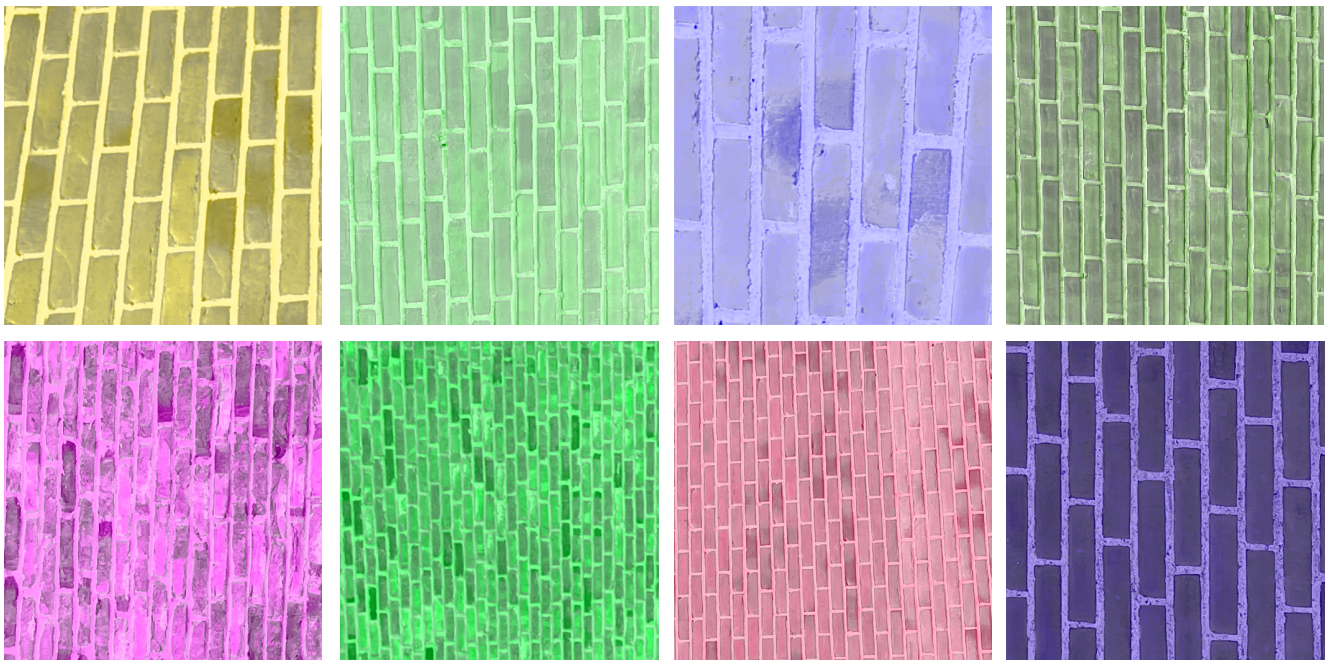


Figure 13. Examples of brick images augmented with RandHue